The Seismic Signature of California's Earthquakes, Droughts, and Floods

T. Clements1∗ and M. A. Denolle2

1) Department of Earth and Planetary Sciences, Harvard University, Cambridge, MA, USA4
2) Department of Earth and Space Sciences, University of Washington, Seattle, WA, USA5
∗Now at U.S. Geological Survey, Moffett Field, CA, USA

This paper is not yet peer reviewed, in the process of reviewing in Journal of Geophysical Researc: Solid Earth

The Seismic Signature of California's Earthquakes, Droughts, and Floods

T. Clements[1*] and M. A. Denolle[2]

[1]Department of Earth and Planetary Sciences, Harvard University, Cambridge, MA, USA
[2]Department of Earth and Space Sciences, University of Washington, Seattle, WA, USA
[*]Now at U.S. Geological Survey, Moffett Field, CA, USA

Key Points:

- Environmental factors considerably change near-surface seismic velocity over decades
- There is a long-term increase in seismic velocities in California due to increased drought conditions
- The decade-long recovery from large earthquakes of sites very close to faults indicate postseismic strain localization and a delayed healing

Corresponding author: Marine A. Denolle, `mdenolle@uw.edu`

Abstract

This study investigates changes in seismic velocities in the period 1999-2021 using about 700 permanent and temporary broadband seismic stations in the state of California. We compute single-station cross-correlations of the ambient seismic noise and use the coda-wave interferometry to measure the changes in seismic velocities (dv/v) using a stretching technique. We focus on the 2-4Hz frequency band and the upper 500 m of the near-surface sensitivity. We discuss dv/v within the context of nonlinear elasticity. We fit models of thermoelastic strains, various hydrological models that diffuse rain water, and slow-dynamics healing models for post-seismic response of earthquakes. In general, we find that both thermoelastic strains and hydrological strains have similar amplitude of impacts on dv/v. We find that the diffusion of rainwater using a drained response in a poroelastic medium explains most of the data. The best fit hydraulic diffusivity are high in the mountains and low in the basin. We find that the largest drop in seismic velocity occurs during the 2004-2005 wet winter, and that the 2011-2016 Drought is characterized by a multi year marked increase in dv/v. We interpret site-specific variations with land subsidence or inflation detected by remote sensing. We also find decade-long post-seismic response of two major earthquakes and bound the time scale of relaxation processes to a few years. Together, we see long-term changes in seismic velocities are showing positive trend over two decades that we can interpret as long term lowering of the groundwater table.

Plain Language Summary

The multi-year droughts and sudden downpours cause stress to the water management and natural hazards in California. This study investigates their impact on the subsurface seismic properties. Large seismic data archives such as reliable permanent seismic networks and large computing capabilities allow for a state-wide, 2-decade long analysis of the changes in the shallow seismic structures. The near-surface seismic velocities in the upper 500 m of the Earth's crust are strongly modulated by annual variations in air temperature and diffusion of rainfall. Due to extreme climate conditions in California, seismic velocities change by up to -2% during a single winter due to rain, and up to 2% during 20 years of progressively drying conditions. The recovery of fault-zone materials near two significant earthquakes, the 1999 Hector Mine and 2010 El Mayor Cucapah earthquakes, indicates a relaxation process that can last decades and that implies characteristic time scales of a few years and a spatial heterogeneity that coincide with deep crustal viscous properties. This study presents passive seismology as a tool to probe Earth's tectono-hydrological processes that are complementary to geodesy and hydrology.

1 Introduction

The state of California is subject to extreme natural events. It hosts infrequent, large magnitude ($M_w \geq 7$) earthquakes (Gutenberg & Richter, 1944; Hutton et al., 2010; Toppozada et al., 2002), multi-year droughts (S.-Y. S. Wang et al., 2017), extreme precipitation events (M. D. Dettinger et al., 2011) and floods (S.-Y. S. Wang et al., 2017), wildfires (Williams et al., 2019), and has the potential for massive landslides (Shreve, 1968) and volcanic eruptions (Miller, 1989). In the last two decades, California's annual precipitation has swung from deluge to drought: the recent 2012-2016 drought was unprecedented in the observational record (Swain et al., 2014), with the lowest three-year rainfall recorded in the last hundred years, while the winter of 2017 was one of the wettest in the historical record (S.-Y. S. Wang et al., 2017). Over this same time period, California hosted three M_w7+ earthquakes: the 1999 M_w7.0 Hector Mine, 2010 M_w7.2 El Mayor Cucapah, and 2019 M_w7.1 Ridgecrest earthquakes.

Extreme environmental and tectonic events often alter the mechanical and hydrological properties of the near-surface to the extent that is geophysically measurable. Strong ground motion from earthquakes can deform, fracture, and liquefy soil in a matter of seconds (Trifunac, 2016). Heavy precipitation during atmospheric river events can cause river levels to rise 5m in a single day (Ralph & Dettinger, 2011). At the same time, over multiple years, hydrological droughts lead to groundwater levels decreasing tens of meters (California Department of Water Resources, 2015), pushing society to rely on pumped groundwater for its water needs (Perrone & Jasechko, 2017). Because the speed of seismic waves depends on the subsurface's mechanical properties, we can use repeated measurements of seismic wavespeeds to infer mechanical changes to the near-surface. *Dynamic* or *time-dependent* seismic wavespeeds for a particular location can be estimated from repeated travel-time measurements (De Fazio et al., 1973; Reasenberg & Aki, 1974; Yamamura et al., 2003). Earthquakes (Poupinet et al., 1984), air guns (Reasenberg & Aki, 1974), electric pulses (Yamamura et al., 2003), explosions (Nishimura et al., 2005) or oscillators (De Fazio et al., 1973) are common seismic sources for travel-time measurements and provide high signal to noise ratio signals but are often infrequent (earthquakes) or expensive to repeat (explosions). Another approach is to use passive, ambient seismic waves and wavefield cross-correlation to extract travel-time measurements. In this case, ocean waves (Webb, 2007; Hillers et al., 2012; Ardhuin et al., 2015) or anthropogenic activities that generate emergent waves (Riahi & Gerstoft, 2015; Diaz et al., 2020) are common sources of the ambient noise field. Because sources of the ambient field are relatively constant over time, the method allows for monitoring near-surface changes over a wide range of time scales from seconds (Bonilla & Ben-Zion, 2021) to decades (Lecocq et al., 2017; Clements & Denolle, 2018; Sens-Schönfelder & Eulenfeld, 2019).

Near-surface monitoring with ambient noise has been employed to investigate various environmental and tectonic forces over the last two decades. Sens-Schönfelder and Wegler (2006) were the first to apply travel-time-based ambient noise monitoring outside the laboratory. They found a striking anti-correlation between groundwater level and seismic wavespeed at Mt. Merapi, Indonesia. The following year, Wegler and Sens-Schönfelder (2007) measured a sudden decrease in seismic wavespeed following the 2004 M6.6 Mid-Niigata Earthquake. Since then, numerous studies have found the significant influence of thermoelastic stresses (Ben-Zion & Leary, 1986; Tsai, 2011; Snieder et al., 2002; Richter, Sens-Schönfelder, et al., 2014; Lecocq et al., 2017), measured and inferred pore-pressure changes (Lecocq et al., 2017; Clements & Denolle, 2018; Q. Y. Wang et al., 2017; Feng et al., 2021; Andajani et al., 2020), tidal stresses (De Fazio et al., 1973; Takano et al., 2017; Mao et al., 2019; Takano et al., 2019; Sens-Schönfelder & Eulenfeld, 2019), earthquake damage near the fault (Brenguier, Campillo, et al., 2008; Froment et al., 2013; Obermann et al., 2014; Taira et al., 2015; Boschelli et al., 2021; Lu & Ben-Zion, 2022), and ground-motion induced damage (Rubinstein, 2004; Viens et al., 2018; Bonilla et al., 2019; Bonilla & Ben-Zion, 2021), atmospheric loading (Gradon et al., 2021), snow loading (Q. Y. Wang et al., 2017; Donaldson et al., 2019), and magmatic intrusion (Brenguier, Shapiro, et al., 2008; Rivet et al., 2014; Brenguier et al., 2011; Obermann, Planès, et al., 2013; Mordret et al., 2010).

Environmental and tectonic forces act at various spatial and temporal scales with varying intensities. Thermoelastic strains, driven by daily and seasonal cycles of surface temperature change, peak at the near-surface (Richter, Sens-Schönfelder, et al., 2014; Meier et al., 2010), though their amplitudes depend on the local spatial wavelength of topography (on the scale of kilometers) (Berger, 1975; Ben-Zion & Leary, 1986). Hydrologic forces have seasonal and long-term temporal components (Sens-Schönfelder & Wegler, 2006; Lecocq et al., 2017; Clements & Denolle, 2018) and their impact on dv/v varies spatially depending on the subsurface hydrological structure (Clements & Denolle, 2018; Mao et al., 2022). In contrast, large earthquakes are infrequent, near-instantaneous at the time scale of seismic measurements, and their impacts are mostly concentrated near the earthquake source (Froment et al., 2013; Lu & Ben-Zion, 2022; Obermann et al., 2014;

Wu et al., 2016), with nonlinear ground motions occurring infrequently in distant basins (Rubinstein, 2004; Peng & Ben-Zion, 2006; Minato et al., 2012; Viens et al., 2018; Bonilla et al., 2019). The effects of these factors on the seismic velocities are often the linear combination of these factors.

This study is the first multi-decadal survey of near-surface seismic velocities across the entire state of California. It first reviews the theoretical framework to interpret seismic velocity changes due to thermoelastic stresses, hydrological loads, and earthquake damages in a nonlinear elastic rheology context. Then, we use 20 years of continuous data recorded at over 700 broadband seismometers and a single-station cross-correlation methodology. We then present a detailed example of the effects of groundwater and thermoelasticity on the modulation of seismic velocities, with calibration using i) groundwater well levels, ii) inference from satellite measurements, and iii) models using three canonical hydrological models. This work then presents the first state-wide scale analysis of changes in the near-surface over two decades of recording. We find the long-term effects of multiple droughts, short-term effects of atmospheric rivers, and multi-scale effects of earthquakes in the western United States on seismic velocities. We also find significant heterogeneity in how seismic velocity responds to these effects, which provides an upper bound for the length scale of heterogeneity for the near-surface poro-thermo-elastic structure.

2 What is dv/v?

2.1 The dv/v measurement

Travel-time measurements with passive seismic sources are often measured within coda waves, which take a circuitous path scattering between the source and receiver by reflecting and diffracting off structural heterogeneities in the Earth (Aki & Chouet, 1975). Scattering reduces the sensitivity of coda waves to the original seismic source, which allows for an increase in sensitivity near the receiver (Dodge & Beroza, 1997). Coda waves sample a broader volume than the direct, ballistic waves and thus are more likely to sample the perturbed medium.

Coda-wave interferometry (CWI) is a technique to infer changes in seismic velocity through travel-time differences measurements in coda waves (Snieder et al., 2002). With the assumption that there is a homogeneous velocity change in the sampling medium, the relative time delay in the coda, dt/t, is related to the relative change in seismic velocity, dv/v, by $dt/t = -dv/v$. Recent work has shown that this relation holds for many realistic scenarios of velocity perturbation (Obermann, Planès, et al., 2013; Obermann et al., 2016; Yuan et al., 2021). dv/v can be measured from increased phase shifts in coda waves as a function of lag time through a linear regression (Poupinet et al., 1984; Lecocq et al., 2014; Mao et al., 2020; Mikesell et al., 2015) or by maximizing the correlation coefficient between a reference and perturbed waveform after stretching the time-axis (Lobkis & Weaver, 2003; Sens-Schönfelder & Wegler, 2006; Yuan et al., 2021). These methods are reviewed and compared in (Yuan et al., 2021). This study uses the time-domain stretching technique to measure dt/t and dv/v at the frequency band 2-4 Hz. We do not investigate or compare with other methods and frequency bands for computational simplicity.

2.2 Relation between dv/v and strain in nonlinear elasticity

While the relation between perturbation in seismic velocities and stresses or strains has been observed and empirically estimated, nonlinear elasticity provides grounds for a theoretical framework. Nonlinear elasticity is an extension of classic elasticity that helps to explain the mechanical defects of real rocks (P. a. Johnson & McEvilly, 1995). In this study, we interpret relative changes in velocity dv/v with nonlinear elasticity. Follow-

Table 1. *dv/v* sensitivity to dilatational strains reported in the literature.

Reference	$\vert\beta\vert$	Geological Context	Strain levels
Hillers, Ben-Zion, et al. (2015)	5×10^3	Air thermal strains	low strains
Wegler et al. (2009)	$1.9 - 2.5 \times 10^5$	Co-seismic damage	high strains
Ueno et al. (2012)	6×10^4	Volcanic, dike opening	moderate strains
Takano et al. (2017)	8×10^3	Volcano, shallow deformation	small strains
Hillers, Retailleau, et al. (2015)	$5 - 10 \times 10^3$	solid Earth tides	small strains
Takano et al. (2019)	5×10^4	solid earth tides	small strains
Mao et al. (2019)	$1 - 2 \times 10^4$	Volcanic context, tidal strain	small strains
Sens-Schönfelder and Eulenfeld (2019)	1.6×10^4	Environmental, tidal strains	small strains
Takano et al. (2014)	6.9×10^4	Volcanic setting, tidal strains	small strains
Donaldson et al. (2019)	160	Volcanic Dike opening	moderate strains

ing equation 5 of (Ostrovsky & Johnson, 2001), the one-dimensional stress-strain relationship containing nonlinear effects can be reformulated as,

$$\sigma = M(\epsilon + \beta\epsilon^2 + \ldots), \tag{1}$$

where M is the second- and third-order elastic modulus, given by 2 and 3 independent components for an isotropic material, and β is the acousto-elastic parameter. In this framework, β can be expressed in terms of the 3^{rd} order Murnaghan moduli as,

$$\beta = \frac{3}{2} + \frac{l + 2m}{\lambda + 2\mu}. \tag{2}$$

Experimental values for β vary widely based on the materials, but generally, β is a large, constant, and negative (Rivière et al., 2015). Reported values for steel are around -10^0 (Hughes & Kelly, 1953), concrete in the range of -10^1 to -10^2 (Schurr et al., 2011; Larose & Hall, 2009; Shokouhi et al., 2010; Payan et al., 2009; Zhang et al., 2012), Barre granite in the range of -10^2 to -10^3 (Nur & Simmons, 1969a), marble around -10^3 (P. A. Johnson & Rasolofosaon, 1996), and Fontainbleau sandstone around -10^4 (P. A. Johnson & Rasolofosaon, 1996). Under nonlinear elastic rheology, the local acoustic velocity can be expressed as (Ostrovsky & Johnson, 2001),

$$v = \sqrt{\rho^{-1} d\sigma/d\epsilon} \approx v_0(1 + \beta\epsilon + \ldots), \tag{3}$$

where v and v_0 are the perturbed and unperturbed velocities. The change in velocity $\frac{\Delta v}{v} = \frac{v - v_0}{v_0}$ due to a hydrostatic stress, σ_{kk}, as a function of the volumetric strain, ϵ_{kk}, then becomes,

$$\frac{\Delta v}{v} = \beta\epsilon_{kk}. \tag{4}$$

β is effectively a measure of the sensitivity of a material's properties to strains. Numerous studies have inferred β using Earth tides to calculate the ratio of dilatational strain to dv/v, as shown in Table 1.

dv/v has also been inferred to be sensitive to shear strain ($\epsilon_{ij}, i \neq j$) generated by strong ground motions, usually during or after a drop in *dv/v*. Dynamic shear strains from strong ground motions are approximated using peak ground velocity and local knowledge of shear wavespeed (Guéguen, 2016). The sensitivity of *dv/v* (e.g. of the shear modulus) to shear strains is largest at surface sensors during the shaking of earthquakes (Bonilla et al., 2019; Bonilla & Ben-Zion, 2021).

Decreases in *dv/v* during strong ground motion have also been correlated to transient dynamic stresses (Richter, Sens-Schönfelder, et al., 2014; Brenguier et al., 2014; Viens et al., 2018; von Seggern & Anderson, 2017; Ikeda & Takagi, 2019). In this case, dynamic stress changes induce the opening and closing of cracks in the subsurface, which results in a change in seismic velocity (Budiansky & O'connell, 1976). Occasionally, *dv/v* has been correlated with strain rate, rather than strain, during slow-slip events when deformation was calculated from an elastic slip model (Rivet et al., 2014).

2.3 Decomposition of *dv/v* as a linear combination of strains

Empirical studies of *dv/v* suggest that *dv/v* can be decomposed into a linear combination of environmental and tectonic time terms:

$$dv/v_{model}(t) = a_0 + a_1 * f_w(t, w_i) + a_2 * f_T(t, t_i) + a_3 * f_q(t, q_i) + f_\epsilon(t), \qquad (5)$$

where $a_i, i \in [0, 3]$ are scalar coefficients, f_w is the hydrological term, f_T is the thermoelastic term, f_q is the earthquake(s) term, and f_ϵ is the combination of unmodeled terms (e.g., instrumental noise). Here, we limit the decomposition to the three terms that dominate the signals of this study. However, other terms such as snow load (Q. Y. Wang et al., 2017; Donaldson et al., 2019), atmospheric pressure (Niu et al., 2008; Olivier & Brenguier, 2016; Gradon et al., 2021) are ignored here. Such linear decomposition has been successfully employed in multi-year studies (Tsai, 2011; Q. Y. Wang et al., 2017; Donaldson et al., 2019; Richter, Sens-Schönfelder, et al., 2014; Feng et al., 2021). Each term is a function of time and of model-specific parameters, which we describe in the following sections.

Coupling among these terms is possible and would invalidate the linear decomposition of equation 5. Earthquake damage often opens cracks in the near-surface and allows for increased groundwater flow (Rojstaczer et al., 1995; Brodsky, 2003; Illien et al., 2022), which temporarily alters the hydrological parameters (increased permeability) that we often assume fixed through time. Sens-Schönfelder and Eulenfeld (2019) models the coupling between tidal and thermoelastic strains.

2.4 Thermoelastic *dv/v*

The thermoelastic term, $f_T(t, t_i)$, corresponds to rock's thermal expansion and contraction due to temporal fluctuations in surface temperature. Berger (1975) gave a solution for thermoelastic strain in a halfspace, where thermoelastic strain attenuates exponentially with depth. Ben-Zion and Leary (1986) found that measured strains in Southern California were well approximated by Berger (1975)'s theory. Under this framework, Richter, Sens-Schönfelder, et al. (2014) derived a relation between *dv/v* and the temperature perturbation at depth. The sensitivity of *dv/v* to changes in surface temperature is positive; the dilating effect of heating counter balances the confinement of rocks (Richter, Sens-Schönfelder, et al., 2014; Lecocq et al., 2017; Rodríguez Tribaldos & Ajo-Franklin, 2021).

There are two dominant periods for surface temperature variations: daily and annual. The daily variation in temperature only affects the shallowest layers, whereas the annual variation in surface temperature has a larger amplitude and diffuses to a greater depth. The long-term increase in temperature may also have a noticeable effect on *dv/v*, as Lecocq et al. (2017) found a long-term increase in seismic velocity over 30 years in Germany.

Following the framework proposed by Richter, Sens-Schönfelder, et al. (2014), we simply use the functional form $f_T(t, ti) = \delta T(t - t_i)$, where $\Delta T(t)$ is the demeaned daily surface air temperature time series at a particular location. We solve for the amplitude a_2 and phase shift t_i using optimization. Because our analysis is limited to a specific frequency band, we do not account for a depth variation in these factors.

2.5 Co-seismic damage and post-seismic relaxation impacts on dv/v

The reduction in seismic velocities during and after a strong motion event is ubiquitous. During the shaking of earthquakes, they can drop by as much as 50% (Bonilla et al., 2019; Bonilla & Ben-Zion, 2021). Within a day after the earthquake, near-surface velocities stabilize down to a few percent reduction in velocity (Wegler & Sens-Schönfelder, 2007; Nishimura et al., 2005; Brenguier, Campillo, et al., 2008; Wegler et al., 2009; Hobiger et al., 2012; Minato et al., 2012; Taira et al., 2015; Viens et al., 2018; Hobiger et al., 2016; Ikeda & Takagi, 2019; Richter, Sens-Schönfelder, et al., 2014; von Seggern & Anderson, 2017), probably reduced from co-shaking levels through a rapid phase of healing. Seismic velocities recover over time, with timescales ranging from days to months or even years to full recovery (Wu et al., 2016; Viens et al., 2018; Marc et al., 2021).

The recovery of dv/v likely occurs over a range of spatial and temporal scales from the micro and mesoscale and from seconds to years, respectively (Snieder et al., 2017). There is debate on whether seismic velocities recover with a logarithmic time dependence (P. A. Johnson & Jia, 2005; Wu & Peng, 2012) or exponential-time dependence (Gassenmeier et al., 2015, 2016; Hobiger et al., 2014; Richter, Sens-Schönfelder, et al., 2014; Viens et al., 2018; Qiu et al., 2020) after strong ground motions. Snieder et al. (2017) proposed a relaxation model that combines both functional behaviors:

$$R(t) = \int_{\tau_{min}}^{\tau_{max}} \frac{1}{\tau} e^{-t/\tau} d\tau, \tag{6}$$

which gives a finite velocity drop at $t = 0$, a logarithmic decay $-ln(t)$ for times within τ_{min} and τ_{max}, and an exponential decay $\exp -t/\tau_{max}$ for periods much longer than τ_{max}. t_{min} and τ_{max} are effectively the shortest and longest characteristic time scale of healing, or slow dynamics (Snieder et al., 2017). We fit this model to find τ_{min} and τ_{max} at selected sites. We only find a few of these sites geographically constrained close to large earthquakes, indicating that the processes involved are particularly localized.

Earthquakes damage the near-fault and near-surface environment by reducing elastic properties under large strain perturbations. Laboratory experiments have been conducted to explain the seismic observations in nature. Changes in velocities near laboratory faults are observed to vary systematically during the seismic cycle (Kaproth & Marone, 2013; Shreedharan et al., 2021) in three distinct phases. In the interseismic, the bulk materials experience an increase in seismic velocities while the fault is locked and the rock sample is loading. In the co-seismic, dilation of the bulk material is interpreted with a two-stage reduction in seismic velocities coinciding with pre- and co-seismic slip (Kaproth & Marone, 2013; Shreedharan et al., 2021). In nature, this corresponds to the drop in seismic velocities observed in proximity to the faults of earthquakes (Brenguier, Shapiro, et al. (2008); Taira et al. (2015), and references therein). A second mechanism for the drop in seismic velocities measured by surface seismometers is the nonlinear elastic response (Bonilla et al., 2019; Bonilla & Ben-Zion, 2021) and visco-elastic or plastic damage to the near-surface sediments due to strong shaking (Nakata & Snieder, 2012; Viens et al., 2018; Boschelli et al., 2021; Lu & Ben-Zion, 2022). After the shaking, Earth materials start to heal, and seismic velocities recover (or at least partially). In the near-surface environment, materials may undergo "slow dynamics" whereby dilated media gradually compress back to their original states, or co-seismically generated cracks start to close (Rubinstein & Beroza, 2005; Snieder et al., 2017). The time scale for the damage recovery is multi-scale (Shokouhi et al., 2017), whereby most of the damage occurs within seconds (Bonilla et al., 2019), a significant portion is recovered within days (Viens et al., 2018) to months (Boschelli et al., 2021). Near the fault, the elastic moduli increase again as the fault interface re-strengthen (growth of the contact areas of asperities) (Shreedharan et al., 2021).

2.6 Hydrological *dv/v*

The relation between seismic velocities and groundwater is often observed as an anti-correlation between *dv/v* and water levels or hydraulic heads when the seismic waves are dominated by shear and surface waves. This is observed in groundwater aquifers (Sens-Schönfelder & Wegler, 2006; Q. Y. Wang et al., 2017; Donaldson et al., 2019; Liu et al., 2020; Clements & Denolle, 2018), water-table levels (Voisin et al., 2016, 2017), subsurface moisture (Illien et al., 2021), river levels (Berbellini et al., 2021; Rodríguez Tribaldos & Ajo-Franklin, 2021), and during the melting period of permafrost (James et al., 2017). The reason might be that below the water table, the hydrostatic pore pressure may reduce effective stress, thus decreasing the seismic velocities (Grêt et al., 2006).

In partially saturated media, seismic velocities are sensitive to small changes in fluid saturation, though this depends on the pore shape (O'Connell & Budiansky, 1974) and the wave type (Garambois et al., 2019). In general, changes in seismic velocities in the shallowest layers, near or above the water table in the capillary fringe, may have contrasting effects on seismic body-wave speed. For example, using active surveys, (Garambois et al., 2019) showed that shear-wave velocities are anti-correlated with groundwater level (or pore pressure) but that P-wave velocities are correlated with groundwater levels. The mechanics of partially saturated low-cohesion geomaterials is complex, it may need to account for the evolution of pore pressure in a highly heterogeneous permeability structure, and changes in the material's chemical composition with mineral hydration (Rodríguez Tribaldos & Ajo-Franklin, 2021).

The impact of hydrology on *dv/v* remains challenging to constrain with a theoretical framework, even below the water table. When *in-situ* measurements of groundwater levels or pore pressure are not available, seismologists often model the pore pressure given surface measurements (e.g., precipitation) but ignore the effects of storage such as maintained aquifers and lakes (Feng et al., 2021). Most studies that approximate groundwater with rainwater diffusion work either in mountainous regions (Feng et al., 2021), in the near-surface environment (Illien et al., 2021) or at the crustal scale (Q. Y. Wang et al., 2017).

In this study, we evaluate three hydrological models used by the seismological community. These models assume unconfined aquifers and measurements below the water table, which we argue is a reasonable assumption in our analysis, given the depth sensitivity of our measurements. During and after rainfall, groundwater levels rise as precipitation percolates into the saturated zone if the soil is already partially saturated (we do not account for cases of drought-induced impermeability of soils). Groundwater levels then quickly fall as pressure gradients induce horizontal flow.

2.6.1 Recession Model

Sens-Schönfelder and Wegler (2006) developed a model for groundwater levels h at time t after precipitation based on the assumption that under a linearized Dupuit-Boussinesq flow, drainage occurs exponentially as,

$$\Delta h(t) = \sum_{i=0}^{n} \frac{P_i}{\phi} e^{(-a(t-t_i))} \tag{7}$$

where ϕ is the porosity and P_i is the amount of precipitation on a previous day i. This model approximates the classic baseflow recession curve $Q = Q_0 e^{-at}$, where Q is the rate of flow, t is time, Q_0 is the flow when $t = 0$, and a is a constant that depends on the time scale of recession (Tallaksen, 1995). The model starts at time $t = 0$. In practice, we take the daily precipitation reduced by the mean $P_i - P$. We empirically found that keeping the mean yield a divergent prediction of Δh as a function of time.

2.6.2 Poroelastic Model

Poroelasticity is a mechanical formulation to couple the constitutive relations between fluid flow and solid mechanical response (Segall, 2010). E. A. Roeloffs (1988) calculated the coupled poroelastic response of a halfspace at depth z due to a surface load of amplitude p_0 as

$$P(z,t) = \frac{B(1+\nu_u)}{3(1-\nu_u)} p_0 erf\left[\frac{z}{(4ct)^{1/2}}\right] + p_0 erfc\left[\frac{z}{(4ct)^{1/2}}\right], \tag{8}$$

where erf and $erfc$ are the error and complementary error functions, respectively, c is the diffusivity of the porous material, t is the time since the load was applied, ν_u is the "undrained" Poisson's ratio, and B is the Skempton's coefficient. B is close to 1 at the surface and rapidly decreases with depth (E. Roeloffs, 1996; Pimienta et al., 2017). The first term on the right hand side of equation 8 is the undrained poroelastic response due to elastic loading, whereas the second term on the right-hand side of equation 8 is the drained poroelastic response due to diffusion. The medium response is "undrained" when there is no fluid flow in response to a change in stress $\Delta\sigma_{ij}$ (Rice & Cleary, 1976). At zero lag time, the response is undrained, while at an infinite lag time, the response is fully drained.

Talwani et al. (2007) modified E. A. Roeloffs (1988)'s model to accommodate the change in pore pressure at depth due to a series of precipitation loads, given by,

$$p_i(z,t) = \frac{B(1+\nu_u)}{3(1-\nu_u)} \sum_{i=1}^{n} \delta P_i erf\left[\frac{z}{(4c(n-i)\delta t)^{1/2}}\right] + \sum_{i=1}^{n} \delta P_i erfc\left[\frac{z}{(4c(n-i)\delta t)^{1/2}}\right] \tag{9}$$

where $t = n \cdot \delta t$ is the number of days since the start of the rainfall time series ($i = 1$). $\delta p_i = \rho g \delta P_i$ is the pore pressure change variation due to precipitation $\delta P_i = P_i - \bar{P}_i$ on day i, where $\bar{P}_i = 1/i \sum_{k=1}^{i} P_k$, This model is popular and researchers have either used the full equation 9, or the drained response only (second term in equation 9), especially for greater crustal depth where the Skempton's coefficient B is small (Rivet et al., 2015; Q. Y. Wang et al., 2017).

2.6.3 Empirical CMDk Model

Recently, Smail et al. (2019) introduced the empirical Cumulative Deviation from the Moving Mean (CDMk) of Precipitation approach to estimate deviations in groundwater levels from precipitation measurements alone. The CDMk method assumes that groundwater levels respond to deficits or surpluses of precipitation in the last k days, where $k >> 365$, which is a rough approximation to Darcy's law. Given a daily precipitation time series, p_i, the CDMk for each day i is simple to compute,

$$CDM_{ik} = \sum_{j=1}^{i} P_i - \bar{P_{ik}} \tag{10}$$

where $P_i - \bar{P_{ik}}$ is the daily deviation from the moving or rolling mean $\bar{P_{ik}} = \frac{1}{k}\sum_{j=i-k+1}^{i} P_j$ of k days. Increasing k increases the memory of groundwater to longer-term trends in precipitation. Smail et al. (2019) found that CDMk of 60 months correlated well to groundwater levels in both bedrock and unconfined aquifers but had no correlation to levels in highly confined aquifers. The CDMk and Talwani et al. (2007) models are similar. In fact, the Talwani et al. (2007) model evaluated at $z = 0$ m converges to the CDMk with $k = \infty$, or just the cumulative deviation from the mean of precipitation.

2.6.4 The effect of a hydraulic head and pore pressure on dv/v

Here, we attempt to determine the effect of an increase in groundwater level or hydraulic head Δh on seismic velocity change dv/v using poroelastic and nonlinear elastic frameworks. The constitutive relations for an ordinary isotropic, linearly elastic solid are,

$$\sigma_{ij} - \frac{\nu}{1+\nu}\sigma_{kk}\delta_{ij} = 2G\epsilon_{ij}, \tag{11}$$

where ϵ_{ij} is the strain tensor, σ_{ij} is the stress tensor, δ_{ij} is the Kronecker delta, G is the shear modulus, ν is Poisson's ratio, and i, j are components of space in three dimensions. Poroelastic theory augments the linear elastic constitutive relation by adding the contribution of pore pressure, p, and the change in fluid mass content per unit volume, m. Following the results of Rice and Cleary (1976), the poroelastic constitutive relations are,

$$2G\epsilon_{ij} = \sigma_{ij} - \frac{\nu}{1+\nu}\sigma_{kk}\delta_{ij} + \frac{3(\nu_u - \nu)}{B(1+\nu)(1+\nu_u)}p\delta_{ij} \tag{12a}$$

$$m - m_0 = \frac{3\rho_0(\nu_u - \nu)}{2GB(1+\nu)(1+\nu_u)}\left(\sigma_{kk} + \frac{3}{B}p\right) \tag{12b}$$

where $m - m_0$ is the change in fluid mass content per unit volume, and ρ_0 is the density of the pore fluid. We follow E. Roeloffs (1996) to derive the relation between hydraulic head Δh, strains, and dv/v. We start with the definition of the Skempton's coefficient, which relates pore pressure, p, to isotropic or volumetric stress σ_{kk} (Skempton, 1954),

$$p = \frac{-B\sigma_{kk}}{3}. \tag{13}$$

Using equation (12a), we can recast equation (13) in terms of the pore pressure due to volumetric strain, ϵ_{kk}, as,

$$p = -\frac{2GB}{3}\frac{1+\nu_u}{1-2\nu_u}\epsilon_{kk}, \tag{14}$$

where we note that a change of hydrostatic pore pressure, Δp, for a given change in groundwater level Δh, is given by

$$\Delta p = \rho_0 g \Delta h \tag{15}$$

where g is the gravitational acceleration at the surface. Substituting equation (15) into equation (14) shows that a change in groundwater level is linearly related to the change in volumetric strain, ϵ_{kk}, as,

$$\Delta h = -\frac{2GB}{3\rho_0 g}\frac{1+\nu_u}{1-2\nu_u}\epsilon_{kk}. \tag{16}$$

Equation (16) is similar to the one found by Riley (1969) for relating the compaction of an aquifer due to the instantaneous lowering of a hydraulic head. The coefficient of proportionality between Δh and ϵ_{kk} in the case of compaction is given by the skeletal specific storage S_{sk} (Burbey, 2001),

$$S_{sk} = \frac{3\rho_0 g(1-2\nu)}{2G(1+\nu)}. \tag{17}$$

Substituting equation (4) into equation (16) then gives a relation for the change in seismic wave speed dv/v as a function of change in groundwater level,

$$dv/v = -\frac{3\rho_0 g}{2GB}\frac{1-2\nu_u}{1+\nu_u}\beta\Delta h \tag{18}$$

and in its reduced form,

$$\begin{aligned} dv/v &= -\frac{S_{sk}\beta}{B}\Delta h & (19)\\ &= -\frac{S_{sk}\beta}{\rho_0 g B}\Delta p, & (20)\end{aligned}$$

where dv/v is proportional to the pore pressure change and thus the hydraulic head change through poroelastic and nonlinear elastic constants.

2.7 Fitting the different models to *dv/v*

Here, we describe our model fitting procedure to determine the influence of the factors described in equation 5. We use the limited memory Broyden–Fletcher–Goldfarb–Shanno (LBFGS) algorithm from the `Optim.jl` multivariate optimization package (Mogensen & Riseth, 2018) to find the best model parameters that minimize the mean squared error between the modeled environmental stresses and measured dv/v. The LBFGS algorithm iteratively solves for the 5 parameters a_0, a_1, a_2, w_1, and t_i, as detailed in Section 2.3. We only solve for the seismic dv/v when the data requires it, i.e., when there are obvious large earthquake signals. We also solve for all hydrological models, including cases that only consider either drained or undrained. In the case of the undrained, drained, and fully-coupled models, w_i is the diffusivity parameter, in m/s^2. For the CDMk model, w_i is the number of days in the moving mean. For the recession model, w_i is the recession parameter, in days^{-1}. All hydrology models assume a diffusion depth of 500 m and a porosity of 0.15. For all models, t_i is the best fitting delay between mean daily temperature and dv/v, in days.

3 Seismic, Meteorological, and Structural Data

In this study, we combine seismic waveform data, meteorological data, and Earth structural data to analyze and interpret of our results.

3.1 Continuous seismic data

Seismic monitoring has occurred in California for nearly 100 years, with digitized measurements starting in 1999 (Hutton et al., 2010). The Southern California Seismic Network (SCSN) and the Northern California Seismic Network (NCSN) contribute the large majority of continuous data in California, though temporary seismic networks, such as the Transportable Array (Meltzer et al., 1999), have provided brief increases in station density. Recently, the Southern California Earthquake Data Center (SCEDC) uploaded its entire seismic archive as a Public Data Set (PDS) on Amazon Web Services (AWS). AWS is an on-demand cloud computing and data storage service with an Application Programming Interface (API) to access data and provision computing resources. The SCEDC archive on AWS totals more than 100 Terabytes (TBs) of seismic data saved as day-long miniseed files (bucket name `scedc-pds`, Yu et al. (2021)). We use the `AWS.jl` Julia language API (`https://github.com/JuliaCloud/AWS.jl`, last accessed 5/1/21) to download available data in California from 1999 to 2021 available at the Northern California Earthquake Data Center (NCSN data center) and the IRIS-DMC into an AWS S3 bucket. We download all of the available data, keeping the channel at each site with the highest sampling rate (i.e., HH* instead of BH* when available). We ignore the stations that have less than one year of continuous data.

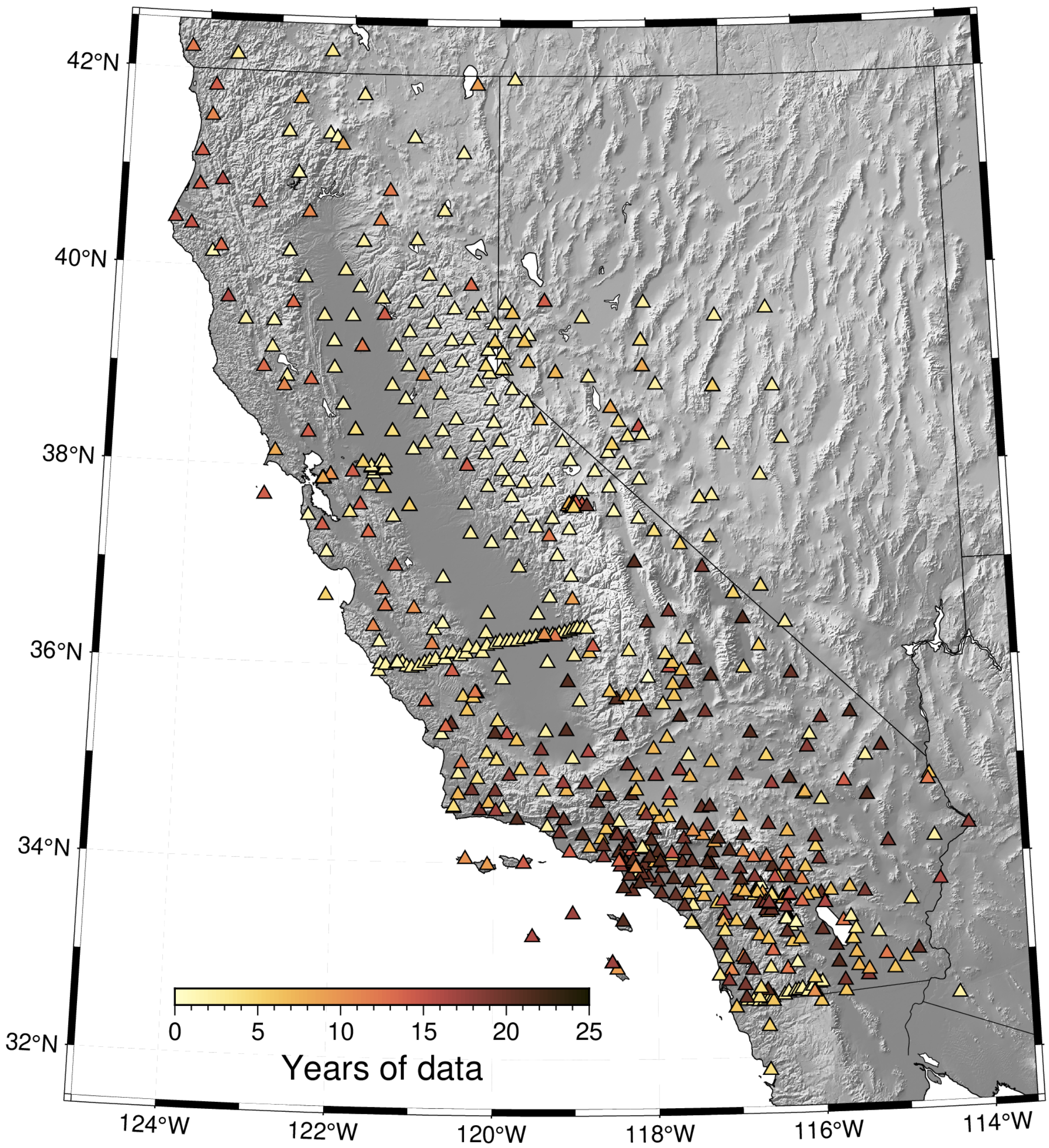

Figure 1. Location of all 718 seismometers used in this study. The time of observations is 1999-2021. Data are from the 8E, AZ, BC, BK, CI, G, II, IM, NC, NN, NP, PY, SB, SN, TA, TO, US, XD, XE, XQ, YB, YN, and YU networks.

Our combined California-wide dataset contains data from 718 unique site locations. Data coverage at individual stations ranges from 1 to 21 years. The total size of the dataset is about 30 TBs. As seen in Fig. 1, California has varying levels of station density that track population and seismic hazard: Southern California is densely instrumented in the greater Los Angeles Basin, while Northern California is densely instrumented along the San Andreas Fault and in the Bay Area. The remaining areas are more sparsely instrumented, with relatively few long-term stations in the Central Valley and the Sierra Nevada mountains.

We develop a cloud-based workflow for ambient-noise seismic data processing. The workflow entails data processing, cross-correlation, and post-processing. We developed several software packages to optimize computing performance on the cloud using the computing language Julia. Once the data products (cross-correlations) are downsized from the original raw data, we migrate the processing back to a single Linux workstation. The entire workflow and algorithms are detailed in `https://github.com/tclements/SCEDCCorr.jl`.

3.2 Single-station ambient-noise cross correlation

This study focuses on shallow depths (upper 500 m) to target typical signals below the water table. We extract measurements of *dv/v* from autocorrelations of the ambient seismic field at individual seismometers. We focus our analysis on the 2-4 Hz frequency band, which has sensitivity down to about 500 m (example shown for CI.LJR in Supplementary Figure S1). Above 1 Hz, anthropogenic sources such as road traffic, trains, manufacturing (Díaz et al., 2017; Schippkus et al., 2020) or intermittent natural forces such as wind or rainfall (Hillers & Ben-Zion, 2011) are the dominant seismic sources. We find that in California, highways are remarkably consistent noise sources. We show the power spectral density of the noise at CI.LJR, which is surrounded by 270° of the highway at Tejon Pass, CA in Figure 2(a).

Ambient seismic noise autocorrelations (ACs) are the cross-correlation of a single component of ground velocity with itself, e.g. (East-East). Single-station cross-correlations (SCs) are the cross-correlations of differing channels, e.g. East-North, North-vertical, and East-vertical, at a single seismometer. Here we choose to focus on SCs functions because of their stability through time (De Plaen et al., 2016; Viens et al., 2018; Feng et al., 2021). Single-station functions ACs and SCs may represent the reflection response from point force sources at the surface (Claerbout et al., 1988; Saygin et al., 2017; Delph et al., 2019; Clayton, 2020; Compaire et al., 2021). The nature of the reflected waves depends on the frequency content and the type of seismic wave (shear or body) that dominates the signals in the cross-correlations (Tkalčić et al., 2020; Viens et al., 2022). The coda of the correlation, however, reveals similar scattering properties as in cross-correlations that have separated sources and receivers, likely similar to the scattering properties of real earthquakes (Wegler & Sens-Schönfelder, 2007), where scattered surface waves dominate in the early coda in layered media (Yuan et al., 2021) and where body waves may have some contributions in weakly depth-varying media (Obermann et al., 2016). Regardless of the nature of the coda wavefield, the tracking of seismic velocity in these correlation functions matches that observed from repeating earthquakes (Machacca-Puma et al., 2019) and receiver functions (Kim & Lekic, 2019).

Before computing cross-correlations, we apply standard pre-processing to the East, North, and vertical components of continuous velocity ground motions in daily chunks using `SeisIO.jl` Julia language package (Jones et al., 2020). To minimize the impact of sensor or data transmission issues, we taper data gaps with a 100-second cosine window. We then remove the mean, the trend, and high-pass filter each channel above 0.4 Hz before removing the instrument response and resampling the data to 40 Hz. We then extract 30-minute long windows, with a 75% overlap between the windows, within the daily trace of seismic velocity (Seats et al., 2012).

We use the SeisNoise.jl package (Clements & Denolle, 2020) to compute the cross-correlations. Each 30-minute window is again demeaned, detrended, and tapered with a 20-second cosine window. We then whiten the data between 0.5 and 19 Hz and apply one-bit amplitude normalization (Bensen et al., 2007). We finally cross-correlate the East-North (EN), East-vertical (EZ), and North-vertical (NZ) components in the frequency domain before transforming them back to the time domain. We stack all cross-correlations within each day using a robust stack algorithm (Pavlis & Vernon, 2010; Yang et al., 2022).

To increase convergence of the cross-correlation functions, we also linearly stack cross-correlations for the previous 90 days.

3.3 Single-station *dv/v* measurements

We measure the change in seismic velocity, *dv/v*, for each station using the stretching technique (Sens-Schönfelder & Wegler, 2006). The stretching technique calculates *dv/v* by measuring the relative time delay, dt/t = -dv/v, by which the time axis of a daily SC waveform must be dilated, or "stretched", to maximize its correlation with a reference SC waveform. Here, we use the linear stack of all SCs as a reference. We calculate *dv/v* in a coda window between 2 and 8 seconds after filtering the single-station cross-correlations from 2 to 4 Hz using a bandpass filter. We estimate six values of *dv/v* for each station: the positive and negative sides of the EN, EZ, and NZ channel SCs. We compute a station average *dv/v* time series by taking a weighted mean across all channels of SCs:

$$CC_{mean} = \sum_{i=1}^{6} cc_i^2 \tag{21}$$

$$dv/v = \frac{1}{CC_{mean}} \sum_{i=1}^{6} cc_i^2 dv/v_i, \tag{22}$$

where cc_i is the correlation coefficient between a daily cross-correlation measurement and the reference cross-correlation after stretching (Hobiger et al., 2014), CC_{mean} is the channel averaged correlation coefficients after stretching. This technique down weights measurements where the stretching of the coda window did not reproduce well the reference coda window. Our final *dv/v* time series for each station are sampled at 90-day resolution due to smoothing.

3.4 Meteorological Data

California has a Mediterranean climate, typified by mild, wet winters and hot, dry summers (Dong et al., 2019) - nearly all rainfall occurs from October to May. In California, annual precipitation totals are heavily dependent on large storms - the wettest 10% of days account for 49% of the annual rainfall (M. Dettinger, 2016).

Groundwater-level time series with daily or sub-daily sampling rates in close proximity to seismic stations are relatively scarce in California. To compensate for this lack of ground truth water levels, we simulate groundwater levels across California using the models described in sections 2.6.1, 2.6.2, and 2.6.3 with daily precipitation levels as input. We extract daily precipitation data from the Parameter-elevation Regressions on Independent Slopes Model (PRISM) dataset. The PRISM dataset incorporates orographic and local climatic effects and covers the conterminous United States from 1981 until today (Daly et al., 2008, 2021). We use the PRISM 4 km × 4 km gridded product of daily precipitation and mean temperature from 1985 to the present for the state of California.

We also use data from the Gravity Recovery and Climate Experiment (GRACE) satellite to constrain large-scale, water-related surface mass changes. GRACE measures time-varying changes in Earth's gravity field at scales of a few hundred kilometers and time scales of about a month (Wahr et al., 1998). The GRACE Liquid Water Equivalent (LWE) product measures the total change in water (snow, surface water, groundwater and soil moisture) that enters and leaves the surface each month with an accuracy within 1.5 cm (Famiglietti & Rodell, 2013). In particular, also use the LWE measurements from the Center for Space Research's GRACE data product (Save et al., 2016) to estimate regional trends in California's groundwater level from 2002-2021.

4 Hydrological *dv/v* analysis at Tejon Pass, CA

We take the site of Tejon Pass in California as a canonical example of our hydrological analysis to discuss California's climatic patterns and impacts on *dv/v*. At Tejon Pass, the variance in annual precipitation is strongly linked to the number and intensity of large storms in a given year. Two time periods stand out from the precipitation record. First, in the winter of 2004-2005, the annual precipitation was over three times the median annual value, and there were eighteen days with large storms. Second, in the 2012-2016 drought, annual precipitation was below the median annual value for five consecutive years, and there were, on average, only three large storm. The years 2012-2016 were without precedence in paleo-climatic history, representing a more than 20,000-year drought event (Robeson, 2015). These swings from deluge to drought are due to the presence or absence of a high-pressure ridge off the west coast(Q. Y. Wang et al., 2017), dubbed the "Ridiculously Resilient Ridge" (Swain, 2015), which prevents large storms from reaching inland California(M. Dettinger, 2016).

We focus our analysis on *dv/v* measurements at station CI.LJR, located in the Tejon Pass between the San Emigdio and Tehachapi Mountains (Buwalda, 1954). Tejon pass is at the intersection of the Garlock Fault and the San Andreas Fault and has been observed geodetically to be dominated by hydrological signals (Hu et al., 2021). CI.LJR has a persistent seismic source at 2-4 Hz, likely due to traffic noise sources from Interstate 5 highway (I-5) that wraps around CI.LJR on three sides. In 2019, ~ 1 vehicle per second entered the Tejon Pass from the North and South, with heavy trucks contributing 25% of incoming traffic (data accessed from https://dot.ca.gov/programs/traffic-operations/censusCalifornia Department of Transit). In the 2-4 Hz frequency band, noise sources are relatively constant day-to-day, though noise power is expected to change through an particular day. Stationary noise sources improve the reliability of the *dv/v* measurements ("Passive seismic monitoring with nonstationary noise sources", 2017). A spectrogram from station CI.LJR at channel NZ is shown in Fig. 2.

Groundwater in the Tejon Lookout flows into the Cuddy Canyon Basin to the West, Peace Valley to the South, and Castac Lake Valley Basin (CLVB) to the North. Flow is likely constrained by the San Andreas Fault to the South and the southern branch of the Garlock Fault to the North. The CLVB is a small ($\sim\ 14km^2$) groundwater basin that provides drinking water for the town of Lebec, CA, and irrigation for nearby agriculture. Groundwater is thought to be unconfined in the entire CLVB. Groundwater wells in the CLVB have declined by 25 m since 2008 due to the combined effects of drought and groundwater extraction for residential use, irrigation, and maintaining the level of Castac Lake (Castac Basin GSA, 2020). CI.LJR is located 2 km away from and 300 m above the nearest pumping well. We use a groundwater well 6 km to the northeast of CI.LJR to estimate trends in groundwater level at CI.LJR ((Castac Basin GSA, 2020), see Fig. 3A). We report that the functional form of the time series of GRACE LWE match well the *dv/v*. However, we later find that the scaling factor between *dv/v* and LWE is particularly station specific without obvious spatial pattern. Therefore, this study will not continue comparing LWE and *dv/v*.

Equation (20) provides us with a proportionality between pore pressure change and *dv/v*. The scalar coefficient that relates the two contains parameters that can be estimated from knowledge of the lithology and seismic properties at the site. We extract a one-dimensional seismic wavespeed and density profile underneath CI.LJR from the Southern California Velocity Model (CVMH v15.1.1, Small et al. (2017)). We guess a shear modulus G between 1 and 10 GPa for a hard, potentially fractured rock material 10 MPa of overburden pressure (Schijns et al., 2018; Saltiel et al., 2017). Using the velocity model

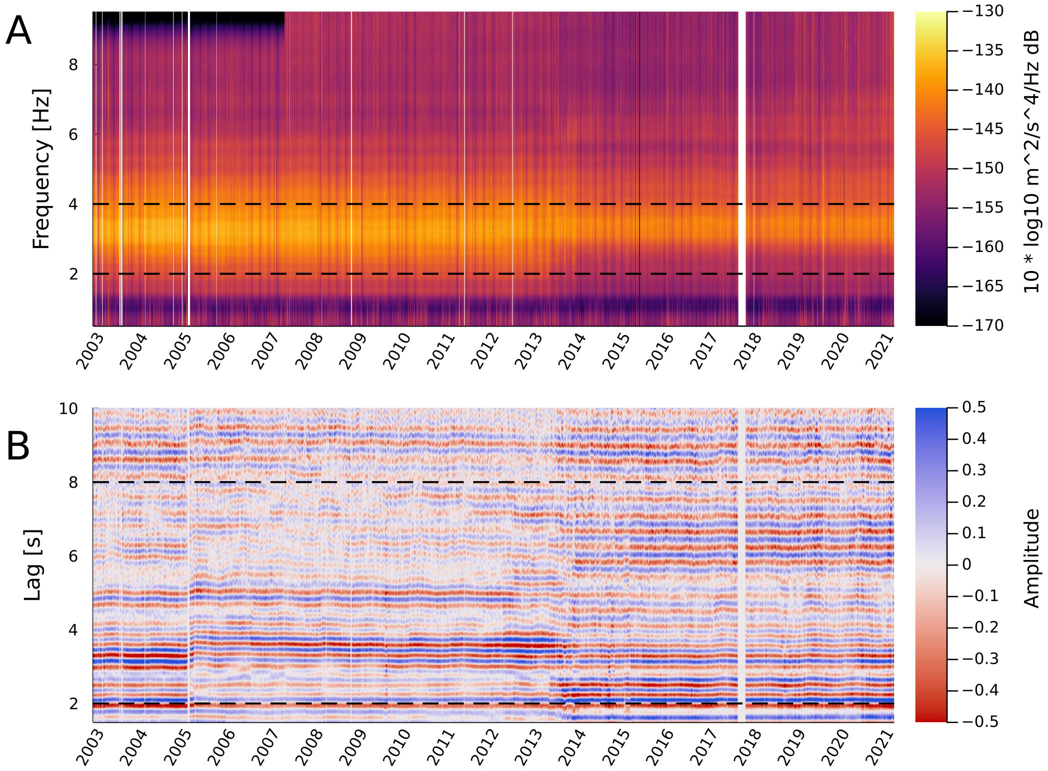

Figure 2. Noise spectrum and single-station correlations at CI.LJR. (a) Daily power spectral density for station CI.LJR. White regions indicate data gaps or instrument failures. (b) Daily North - vertical single-station cross-correlation for station CI.LJR from 2003-2021 for lag times $\tau \in [2, 10]$ seconds in the 2-4 Hz frequency band with amplitude scaled by τ.

from the CVMH would yield $G = 20$ GPa, but we argue that it is too high of a value given the results of Schijns et al. (2018) and Saltiel et al. (2017) and given the large uncertainties of the velocity models at these depth (and topography). We use $\nu = 0.25$. The Skempton coefficient B at $H = 200$ m depth, an overburden pressure $\sigma_n = \rho g H = 5$ is between 0.5 and 0.8 (taking 0.65 as the value) (Hart & Wang, 2010; R. Makhnenko & Labuz, 2013; R. Y. Makhnenko & Labuz, 2016). Using these values, $g = 9.81 m/s^2$, and $\rho_0 = 1000 kg/m^3$ for the pore fluid density, gives values of S_{sk} in the range $1.9 \times 10^{-7} - 1.9 \times 10^{-6}$ m^{-1}, much lower values than reported in sedimentary basins Central California (e.g. $S_{sk} = 2.84 \times 10^{-4} m^{-1}$, Ojha et al. (2018)) but that is reasonable compared to the mean specific skeletal storage found for Granite and fractured igneous rocks (Kuang et al., 2020).

Empirical estimates of β using modeled strain and measured dv/v have found $|\beta|$ ranging from $1 \times 10^3 - 6.9 \times 10^4$ (Takano et al., 2014; Sens-Schönfelder & Eulenfeld, 2019; Mao et al., 2019). At CI.LJR, for a $\Delta h = 5$ m groundwater level change is equivalent to a 2% change in velocity. Taking equation (19), we find that a range of $|\beta|$ of $-13.7 \times 10^3 - - -1.37 \times 10^3$ explains the relation between our measured dv/v and the change in groundwater level at a well in the CLVB 6 km from CI.LJR, as shown in Figure 3. This $|\beta|$ is over an order of magnitude higher than the $\beta = -2.2 \times 10^2$ value reported by Nur and Simmons (1969b) for Barre granite in a laboratory, which suggests that the groundwater level change at CI.LJR is a factor of 10 or so less than in the CLVB. Fur-

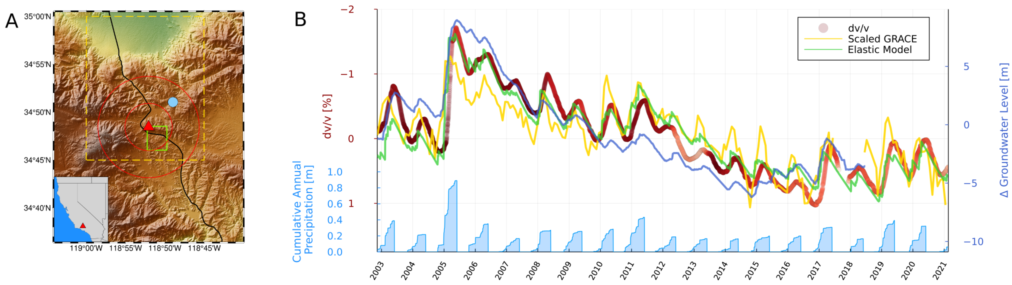

Figure 3. ***dv/v* and groundwater at station CI.LJR**. (a) Location of the seismic station CI.LJR (red triangle). The green rectangle denotes the 4 km x 4 km precipitation grid cell from the PRISM dataset. The black line indicates the path of Interstate 5 through the Tejon pass. The red circles approximate the limit of spatial sensitivity of CI.LJR autocorrelation at lag times of 2 and 8 seconds, respectively. The filled blue dot indicate the position of a groundwater monitoring well in the CLVB. The gold dashed rectangle denotes the 0.25° x 0.25° grid cell from CSR GRACE/GRACE-FO RL06 version 2 Liquid Water Equivalent (LWE) dataset. (b) *dv/v* (red dots colored by CC_{mean}, equation (21)), scaled elastic model of groundwater levels from precipitation (lime green), scaled (and negated) GRACE LWE, cumulative annual water year precipitation (Oct 1 - June 1) for PRISM grid cell containing station CI.LJR, groundwater level change (blue) for well 6 km northeast of CI.LJR, all shown as a function of time in years.

ther measurements of Murnaghan's constants in a wide variety of rocks will lead to better constraints on β.

We fit the pore-pressure models described in sections 2.6.1, 2.6.2, and 2.6.3 against the *dv/v* measurements at CI.LJR. All models suggest a long-term memory of the past precipitation - the best fitting k for the CDMk model is 2,819 days or 7.7 years (Pearson correlation coefficient with -dv/v = 0.97), while the best-fitting a constant for the recession model is 0.0008 days^{-1}, or a half-flow period of $\sim$ 900 days (Pearson correlation coefficient with -dv/v = 0.97). The fully-coupled poroelastic model of Talwani et al. (2007) does not fit the observed -dv/v, though a purely undrained model, obtained by disregarding the drained response in equation (2.6.2), does well at zero lag (Pearson correlation coefficient with -dv/v = 0.96). The best diffusivity constant found with the undrained model is $c = 0.0038\, m^2 s^{-1}$, which indicates a slow flow and a value that falls between the range of intact and fractured igneous rocks (E. Roeloffs, 1996). In this particular case, this strongly suggests that *dv/v* at 2-4 Hz at CI.LJR responds to the load due to precipitation and not the diffusion of the rainwater. We show the equivalent fit for other hydrological models in Supplementary Figure S2.

5 California-wide analysis

We now extend our analysis to the entire state of California. We find significant site-to-site variability in the amplitudes and temporal evolution of the *dv/v* time series. In fact, the standard deviation of *dv/v* is as high as 0.5% (See supplementary Figure S3).

At sites other than CI.LJR, thermal, and tectonic effects may also play a role. The relative contributions between the tectonic, thermal, and hydrological strains vary across sites. The spatial coherence between these effects is related to the location and intensity of the events. For instance, the deluge of precipitation in the winter of 2004-2005 lowered seismic velocities across most of Southern California (M. D. Dettinger et al., 2011), while the effects of tectonic events are confined within the region of extreme ground motions.

5.1 Goodness of fit for the hydrological and thermoelastic models

We fit the hydrological and thermoelastic models at the 647 sites with at least two years of continuous recordings. We report the explained variance values when minimizing the L1 norm (absolute residuals) and the L2 norm (squared residuals) and show them in Supplementary Table S1. We find that the performance of the L1 or L2 norms is similar, meaning that outliers from our *dv/v* time series does not affect our model fitting. Overall, the *drained hydrological* model better fits to 48% of the sites. It also has the best explained variance over the entire sites (0.49). Both the *CDMk* and the *baseflow* models explain each 18% of the data. The *elastic* and *fully-coupled* poro-elastic models each explain less than 7% of the data. We conclude that the *drained* model is preferred overall, with some exceptions (e.g., CI.LJR was best explained by the "elastic" undrained poroelastic model). The remaining and unexplained variance may arise from unmodeled long-term trends, unmodeled tectonic signals, and likely instrumental issues). That said, even if the explained variance is not high, hydraulic diffusivity in the drained model shows a spatial pattern: basin sites tend to have lower diffusivity values (see Supplementary Figure S4), which can be explained by longer rainwater retention or temporary storage of the groundwater in the shallow aquifers of sedimentary basins.

5.2 What dominates between thermal and hydraulic effects

At most sites, the *dv/v* time series is simply a linear combination of temperature and hydrological effects. Here, we choose the drained hydrological model to represent the hydrological effects. The best-fit phase lag to the temperature model is, on average 70 days, relatively consistently throughout the state. There is no spatial pattern where lags would be greater or lesser. This value fits relatively well with previous studies (Tsai, 2011). We estimate the relative contribution of the hydrological and thermal effects on *dv/v* by fitting both terms in the time series and analyzing their relative contributions as the ratio $R_T = a_2/(a_1 + a_2)$ in equation (5).

In general, seasonal thermal effects are important (see Fig. 4). This finding differs from previous studies that found mostly groundwater signals (Sens-Schönfelder & Wegler, 2006; Clements & Denolle, 2018), which we attribute to the higher frequency content (Donaldson et al., 2019) and thus a shallower sensitivity. We report that the relative contribution does not correlate with Vs30 (data from `https://earthquake.usgs.gov/data/vs30/`, last accessed 5/1/21), or elevation, or nor does it present a any particular spatial structure.

There is a strong spatial variability in whether thermal or hydrological effects dominate the change in seismic velocities. An example of such heterogeneity is two sites at the edge of the Salton Sea. At station CI.RXH, located 100 m inland from the southeastern edge of the Salton Sea, *dv/v* has been steadily increasing since 2005 as sea levels have dropped more than 2 m, as shown in Figure 5B. However, just 35 km away, station CI.SAL in Salton City exemplifies the nearly perfect periodical change in *dv/v* modulated by (see Fig.5C).

5.3 Extreme climatic effects: multi-year droughts and atmospheric rivers

After removing the effects of temperature in the *dv/v* time series, we now analyze the hydrological effects. Our measurements exhibit two time scales of response, a short-term that is sub-seasonal and a long-term that lasts multiple years.

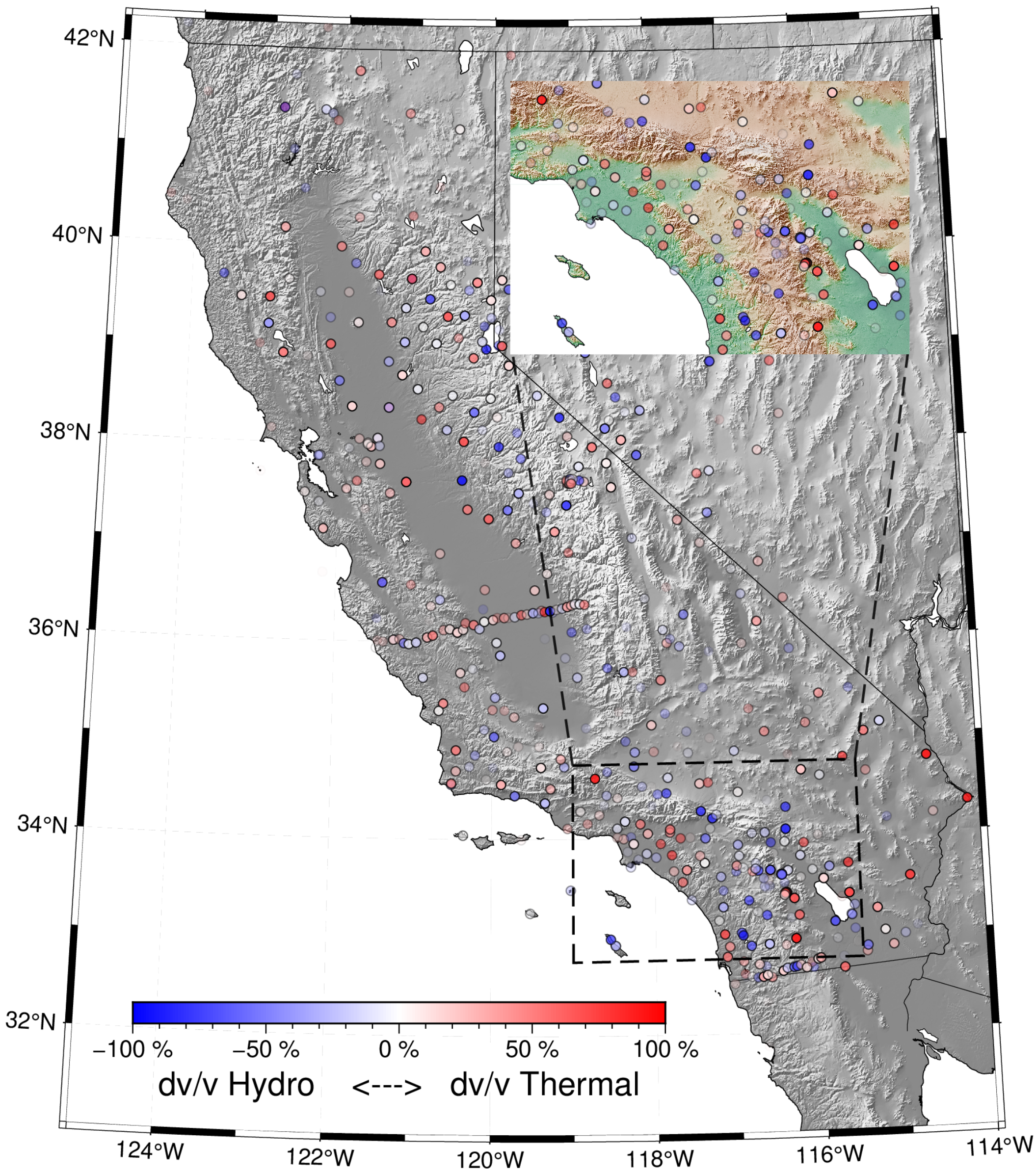

Figure 4. Mixing ratio of fitted dv/v between the hydrological and thermal terms, $R_T = a_2/(a_1 + a_2)$. R_T is red when the temperature dominates the variations in dv/v and blue when the hydrological model dominates. The transparency level is equal to the explained variance of the model.

5.3.1 Winter 2005

Atmospheric rivers bring large amounts of precipitation to California over single storms. They frequently occur during La Niña years. While atmospheric rivers refill surface water reservoirs in California, they also bring hazards through flash flooding, reservoir overflows, and increased landslide activities. The winter of 2004-2005 brought record-setting rainfall to Southern California, with 11 separate storms sweeping across the region in 6 months (Ralph et al., 2011; National Oceanic and Atmospheric Administration, 2005). Cumulative rainfall for that winter was three times greater than the mean from 1985 to 2021. Groundwater levels in the San Gabriel Basin, a managed unconfined aquifer in the greater Los Angeles area, increased by 20 m in response to the extreme precipitation leading to a significant decrease in *dv/v* at seismic stations in the San Gabriel Valley (Clements & Denolle, 2018) and vertical uplift of 4 cm (King et al., 2007). At seismic station CI.LJR, our measured *dv/v* decreased by more than 1% following a set of storms on December 27^{th}-29^{th}, January 2^{nd}-4^{th}, and January 7^{th}-11^{th} and more than 0.85% following a single storm on February 17^{th}-23^{rd}. Overall in California, most seismic stations experienced a decrease in seismic velocity during the winter of 2004-2005 (Fig. 7(a)).

We now evaluate the impact of winter 2005 on the seismic velocities over stations that recorded the event. *dv/v* is typically positive during the winter and negative in the summer. The crest-to-crest variations between the winter maximum (10/1/2004-5/1/2005) and the summer minimum (5/1/2005-10/1/2005) are measured as $p2p = \max(dv/v_{winter}) + \min(dv/v_{summer})$. Given the spatial heterogeneity in *dv/v* variability, we normalize $p2p$ with the mean yearly $p2p$ at each site. We use similar metrics to quantify the variability in cumulative precipitation as the ratio of the cumulative precipitation during that winter with the yearly mean cumulative precipitation between 1985 and 2020.

Figure 7 compares these measures of extreme events between *dv/v* and precipitation in winter 2005. A negative value indicates a large drop in *dv/v* relative to natural variability. A positive value indicates a small drop in *dv/v* relative to natural variability. The magnitude of $p2p$ during the winter 2004-2005 event is comparable to that observed in the distance of earthquakes (Obermann and Hillers (2019) and references herein). These perturbations cannot come from earthquakes since no M $>$ 5 earthquake occurred within Southern California from October 2004 to May 2005. In general, sites in areas of abnormally large rainfall experience a larger velocity drop (Figure 7(a)). This correlation happens mostly in southern California. Northern California experienced average precipitation that winter, and stations on the coast also exhibited a normal response.

5.3.2 The 2011-2016 Drought

In contrast, between 2005 and 2017, the following decade experienced two major droughts, the first from 2007-2009 and the second from 2011-2016. We explore here the latter. After removing the thermal effects in the *dv/v* times series, we estimate the multi-year effect using linear regression on *dv/v* and explore the spatial patterns in the slope of the linear regression. We use the `GLM.jl` package and the linear-regression function. To quantify the drought, we calculate the yearly mean cumulative precipitation over the 2011-2016 drought and the 1985-2020 baseline periods and divide the two. (Figure 7(b)) compares both *dv/v* and the drought metric. Overall, the long-term increase in *dv/v* spatially correlates with areas of significant rain deficit. The long-term increase happens mostly in Southern California and in northern and some parts of the Central Valley.

The San Joaquin Valley in California does not have a dense network of broadband seismometers. Therefore we are missing data in areas of greatest subsidence (Carlson et al., 2020). Two stations are near subsidence bowls detected and imaged by InSAR measurements (Carlson et al., 2020). The station in Visalia, CI.VOG, is nearby one of these, and experienced some of the fastest subsidence in the basin, about 6 cm during that period (Hammond et al., 2016; Blewitt et al., 2018; Carlson et al., 2020). The change in velocity is modest (CI.VOG, 0.05% / year), with an expected pore pressure change of 10 kPa/year as estimated from about -1 m/year hydraulic change from shallow ($\tilde{2}0$ m depth) wells (Carlson et al., 2020). The station in Bakersfield CI.BAK is at the edge of a secondary subsidence bowl, experiencing as well an increase (0.12%/year), and is near a well that had a major drawdown between 12/2006 and 1/2016 of about -3 m/year as measured from a deep water well (300m depth), leading to a possible change in water pressure change of 35 kPa/year (Carlson et al., 2020). On the other hand, station CI.VES is in between these two subsidence bowls, and is experiencing a decline in seismic velocities during that time period (-0.07%/year). The site may be in an area with no estimated changes in pore pressure and volumetric strain change (see Figure 4a of (Carlson et al., 2020)). Carlson et al. (2020) predicts an increase in tension (positive dilatational strains) near Porterville and Pixley, which could explain the negative slope of *dv/v* seen at CI.VES.

We report that the two stations located nearby the dams of large reservoirs, Oroville (BK.ORV) and Lake Isabella (CI.ISA), are quite noisy but show a positive slope (an increase of *dv/v*) during the drought. BK.CMB is located upstream of Lake New Melones; *dv/v* may also reflect the fluctuation in water-table and lake levels (decreasing over the 2012-2016 drought).

Mammoth Lakes Mountain has a particularly large increase in seismic velocities during the drought. Vertical uplift of the Long Valley Caldera system has been detected using GPS (Borsa et al., 2014; Hammond et al., 2016) and interpreted as an extension or positive dilatational strain rates (Klein et al., 2019). A positive dilatation could imply a decrease in *dv/v*. However, the inflation of the volcanic edifice is not related to hydrological unloading but rather an injection of magma in the deep plumbing system (Montgomery-Brown et al., 2015). Therefore, there is no contradiction in interpreting the increase in shallow seismic velocities observed from our *dv/v* measurements with a reduction of shallow pore pressure.

K. M. Johnson et al. (2020) measured the subsidence rates of the Santa Barbara coastline and the Ventura Basin. Stations located in these areas of subsidence (CI.MOP, CI.STC, CI.SBC) exhibit a strong positive slope in *dv/v* with almost 1% change during the 2012-206 drought, though the increase is sustained over most of the seismic record (see Figure 8). CI.SBC has experienced a sustained and constant increase in seismic velocity from 1999 until 2020.

5.3.3 2002-2021

Because of the prolonged droughts compared to wet periods, the long-term change in seismic velocities reflects the California's long-term change in water levels. This change particularly impacts Southern California. We show in Figure 8, that *dv/v* increased up to 2% between 2002 and 2020 at stations in the Los Angeles area. A short atmospheric river in 2017 brought much-needed rain to Southern California (Wen et al., 2018) but represented only a brief interlude in the long-term increase in *dv/v* since 2002. *dv/v* remains stabilized at its 2016 end-of-drought level from 2017-2020. We compare these *dv/v* changes with the 2002-2021 change in LWE from GRACE. GRACE has a much lower resolution (see Fig. 3a). Therefore the spatial pattern we observed with the *dv/v* may vary on a site basis with LWE. Figure 8b shows the *dv/v* time series against LWE time series extracted in the grid cell closest to the station location and scaled by a factor of 1% dv/v = -20cm LWE. Sites in basins have a larger *dv/v* response with respect to the LWE time series (CI.LFP, CI.RIO, CI.LGB, CI.HLL) than mountainous sites (CI.DEC, CI.VCS, CI.SPF, CI.MWC). Overall, the rate of *dv/v* increase is highly anti-correlated with the rate of decrease in LWE (Fig. 8) and the precipitation deficit (Fig. 7).

5.4 Extreme tectonic events

In this step, we remove the modeled hydrological and thermoelastic terms of *dv/v* from stations nearest to known faults that have hosted earthquakes since 1999. The residual *dv/v* times series are, therefore, due to unmodeled components (e.g., instrumental noise) and earthquake effects.

In California's inland areas, M 6 earthquakes occur on average every three years. Several M6+ earthquakes have been studied in detail, the M6.0 2014 Napa Earthquake (Taira et al., 2015), and the M6.0 2004 Parkfield Earthquake (Brenguier, Shapiro, et al., 2008; Wu et al., 2016) for example, that exhibited velocity drops less than 0.1% at seismic frequencies of about 1 Hz.

The variability in *dv/v* after removing the thermoelastic and hydrological model remains high. The standard deviation of the residual *dv/v* time series have a median standard deviation of 0.19% and a mean of 0.25%. We use the median standard deviation as a measure of data error $\sigma = 0.19$. Furthermore, the cross-correlations are averaged over a day, and the *dv/v* times series are smoothed over 90 days. Therefore, our analysis is not appropriate to explore the earthquake damage of the M6 and lower earthquakes.

Nevertheless, we analyze the effects of three major earthquakes: the 1999 M7.1 Hector Mine, 2010 M7.2 El Mayor Cucapah, and the 1999 M7.1 Ridgecrest earthquakes. Each had a station close to the northern rupture terminus: CI.HEC, CI.WES, and CI.JRC2, respectively. These stations are in the near-field of the source, and peak ground velocity values exceeded 20 cm/s, likely too large for the medium to respond in a linear elastic regime.

All stations experience a significant drop in *dv/v* immediately following the earthquake (Fig. 9). The velocity drop is $\approx 1.5\%$ for CI.HEC and CI.JRC2 and $\approx 2.5\%$ for CI.WES. These are reasonable values compared to other studies of these earthquakes (Boschelli et al., 2021; Lu & Ben-Zion, 2022) or greater than others that used stations more distance from the source (Taira et al., 2015; Mao et al., 2020). Because of the relatively low temporal resolution, we likely largely underestimate the maximum drop experienced during and quickly after the shaking (Bonilla et al., 2019; Shokouhi et al., 2017).

Nevertheless, we can model the relaxation of *dv/v* using model of Snieder et al. (2017). We use the same optimization algorithm as the fit of the thermal and hydrological models (LGFBS, Mogensen and Riseth (2018)). Studies have used either an exponential (Gassenmeier et al., 2015, 2016; Hobiger et al., 2014; Richter, Sens-Schönfelder, et al., 2014; Q. Y. Wang et al., 2017; Viens et al., 2018) to simulate post-seismic healing, indicating that the healing starts directly after the earthquake. The exponential response would be equivalent to assuming $t_{min} = 0$ in the healing model. We find that such a condition yields a poorer fit to the data. Instead, we fit for t_{min} in addition to t_{max}. We find that both Bayesian Information Criterion and Akaike Information Criterion are lower for all three fits at HEC, JRC2, and WES when introducing t_{min} as an additional parameter and considering the errors in *dv/v* as Gaussian and of variance σ.

We find that t_{min} is 0.6, 2.9, and 8 years for Ridgecrest, El Mayor-Cucapah, and Hector Mine, respectively. We find that t_{max} is 5.6 and 18 years for El Mayor-Cucapah and Hector Mine. The best fit t_{max} for Ridgecrest reached the upper bound of the allowed values. Therefore we consider it unconstrained and too early in the healing phase.

Post-seismic phenomena include i) afterslip attributed to a decelerating slow-slip on the fault, ii) visco-elastic relaxation of the lower crust and upper mantle, and iii) poroelastic effects typically close to the fault (Gonzalez-Ortega et al., 2014). Independent Component Analysis can separate the contributions of these phenomena on geodetic times series of surface displacements (Gualandi et al., 2016; Gualandi, Avouac, et al., 2020). Gualandi, Liu, and Rollins (2020) also infer a 7-year visco-elastic relaxation, and we interpret this as our t_{max} of 5.6 years. Both ii) and iii) induce particular seismicity that together form the sequence of aftershocks. Gualandi, Avouac, et al. (2020) find that the shallow afterslip of the 2010 El Mayor-Cucapah earthquake lasted up to 8 months. Afterslip and ground motions from the aftershocks may be two mechanisms that would delay the onset of the *slow dynamics*, the healing of the damage materials (Sawazaki et al., 2018). This phenomenon might mostly affect the shallowest, indicating a slower recoupling of the fault.

The time scale to recovery for Hector Mine is 2-3 times longer than that of El Mayor-Cucapah. We find this by fitting the healing model (eq. 6). It is also visible in Figures 9C and D. Such difference in time scale is interpreted by Gualandi, Avouac, et al. (2020) that the viscosity near El Mayor-Cucapah is about half of the value of the viscosity underneath the Mojave Desert.

Finally, only a few stations experience these changes in seismic velocities. Given our single station measurements and shallow depth sensitivity, we may measure a multi-year post-seismic response in the fault zone that would be difficult to measure using conventional remote sensing technique: a relaxation process localized near the damaged fault zone and in the shallow crust.

6 Conclusion

We measure relative seismic velocity changes, dv/v across California using single-station cross-correlations from 1999 to 2021. dv/v time series in the 2-4 Hz frequency has a remarkable sensitivity to near-surface changes. Temperature and possibly pore pressure have been the dominant signals in dv/v in California since 1999. We generally find a long-term increase in velocity that we interpret in the long-term lowering of groundwater levels in California, only punctuated by drops in velocity from groundwater recharge due to large storms. This temporal pattern is most coherent in Southern California's coastal basins. A drained poroelastic model at most sites explains the hydrological term of dv/v. Since we do not model groundwater storage but simply rainwater diffusion, we find that effective diffusivity is low in sedimentary basins compared to mountainous regions.

We have highlighted sites of particular hydrological or tectonic interest. In the Central Valley, despite sparse measurements, we interpret the positive and negative slopes in terms of the spatial heterogeneity in subsidence and groundwater drawdown pointed out by Carlson et al. (2020). The Coastal Santa Barbara coast and Ventura basins are undergoing land subsidence, which we can interpret as a decrease in the water table level. We also compare dv/v (spatial resolution of ≈ 500 m) with Liquid Water Equivalent (spatial resolution of ≈ 400 km). We find that dv/v overpredicts LWE at basin sites, and the opposite is true in mountain sites. This correlation should be investigated further. One could conceive a topography-dependent correction for LWE measurements between basins (where groundwater is stored) and mountains (where groundwater drains) derived from ambient-noise seismology.

The tectonic signals in this study's dv/v measurements show that the near-source relaxation process has a finite range of characteristic time scales, between about one to ten years. The lack of visible tectonic effects at other stations indicates that these shallow processes are proximal to the fault. We also find that the spatial difference in time scales can be explained by the spatial variations in crustal and mantle viscosity. We have not coupled the hydrological terms with the tectonic signals as did Illien et al. (2022). Our approximation may be valid in the cases of southern California earthquakes, given the low water table and occurrence during dry periods. Still, they may be important in northern California or during wet winters.

Turning dv/v measurements into groundwater levels remains a challenge. First, separating the contribution from thermoelastic stresses and tectonic damage is necessary before interpreting hydrological signals. Second, the uncertainties in hydrological parameters such as specific storage and Skempton's coefficient hinder the spatial extrapolation of our measurements. Another limitation is that our hydrological modeling is very basic: the groundwater budget is simplified by the load and diffusion of rainwater. Our modeling only accounts for water storage by means an effective diffusivity, which is low in groundwater basins. Our modeling ignores evapotranspiration: extreme temperatures were thought to account for 8-27% of the drought's moisture deficit (Williams et al., 2015).

Furthermore, the frequency band chosen here only permits shallow estimates of structural changes. Clements and Denolle (2018) and Mao et al. (2022) find that inter-station measurements and lower frequency bands provided more directly the change in velocity with measured groundwater aquifers, which are less affected by thermoelastic stresses. An additional challenge is that the sensitivity of *dv/v* to the various stresses varies spatially without an obvious pattern, which we interpret as strong spatial heterogeneity of this upper layer.

Regardless of the aforementioned limitations, there remains opportunities to combine passive seismology with hydrological and geodetic studies. Direct comparisons between *dv/v* and groundwater wells (Sens-Schönfelder & Wegler, 2006; Clements & Denolle, 2018; Kim & Lekic, 2019), GPS (Tsai, 2011; Clements & Denolle, 2018), InSAR (Mao et al., 2022) present opportunities for future monitoring of the near-surface.

Open Research

The scripts to reproduce this work are available `https://github.com/tclements/Clements-Denolle-2022`. The cloud computing toolbox we developed is available here `https://github.com/tclements/SCEDC.jl`. The dv/v time series and all data to repoduce the study are stored on Zenodo (`https://zenodo.org/record/5794562`). The groundwater well data around CI.LJR is from the Groundwater Sustainability Plan for Castac Lake Valley (Castac Basin GSA, 2020). GRACE data for the Liquid Water Equivalent was extracted from `http://www2.csr.utexas.edu/grace/RL06_mascons.html`. Precipitation and surface temperature data were downloaded from the PRISM Climate Group `https://www.prism.oregonstate.edu/`. The seismic velocity profile was extracted from the SCEC cvmh model and the surface-wave sensitivity kernels were calculated using Computer Program in Seismology codes `https://www.eas.slu.edu/eqc/eqccps.html`. Ground motion data and focal mechanisms for the Ridgecrest, Hector Mine and El-Mayor-Cucapah were downloaded from the USGS Earthquake archive `https://www.usgs.gov/programs/earthquake-hazards/earthquakes`. The seismic networks used in this work are: doi:10.7914/SN/8E, doi:10.7914/SN/AZ, doi:10.7914/SN/BC, doi:10.7914/SN/CI, doi:10.7914/SN/G, doi:10.7914/SN/II, doi:10.7914/SN/IM, doi:10.7914/SN/NC, doi:10.7914/SN/NN, doi:10.7914/SN/NP, doi:10.7914/SN/PY, doi:10.7914/SN/SB, doi:10.7914/SN/SN, doi:10.7914/SN/TA, doi:10.7914/SN/TO, doi:10.7914/SN/US, doi:10.7914/SN/XD, doi:10.7914/SN/XE, doi:10.7914/SN/XQ, doi:10.7914/SN/YB, doi:10.7914/SN/YN, doi:10.7914/SN/YU.

Acknowledgments

We thank Julian Schmitt for downloading the data from Northern California, Xiaotao Yang for introducing us to the robust stacking technique, Kurama Okubo, Jared Bryan, Loïc Viens, Laura Ermert, and Congcong Yuan for discussions on *dv/v* and their models, Ellen Yu and the staff at the Southern California Earthquake Data Center for uploading and maintaining the Public dataset, Jim Rice for his lectures and discussions on poroelasticity, and Brendan Meade for discussions on the Julia programming language. Authors contributions: Conceptualization: MD, TC; Data curation: TC; Formal Analysis, TC, MD; Funding acquisition: MD, TC; Investigation: TC, MD; Methodology: TC, MD; Project administration: MD; Resources: MD; Software: TC; Supervision: MD; Validation: MD; Visualization: TC, MD; Writing - original draft: TC; Writing - review and editing: MD, TC. This research was partially funded by the David and Lucile Packard Foundation (MD) and the Harvard Data Science Initiative (MD, TC).

References

Aki, K., & Chouet, B. (1975, 8). Origin of coda waves: Source, attenuation, and scattering effects. *Journal of Geophysical Research*, *80*(23), 3322–3342. Retrieved from `http://doi.wiley.com/10.1029/JB080i023p03322` doi: 10.1029/JB080i023p03322

Andajani, R. D., Tsuji, T., Snieder, R., & Ikeda, T. (2020). Spatial and temporal influence of rainfall on crustal pore pressure based on seismic velocity monitoring. *Earth, Planets and Space*, *72*(1), 1–17.

Ardhuin, F., Gualtieri, L., & Stutzmann, E. (2015). How ocean waves rock the Earth: Two mechanisms explain microseisms with periods 3 to 300s. *Geophysical Research Letters*, *42*(3), 765–772. doi: 10.1002/2014GL062782

Bensen, G. D., Ritzwoller, M. H., Barmin, M. P., Levshin, A. L., Lin, F., Moschetti, M. P., ... Yang, Y. (2007). Processing seismic ambient noise data to obtain reliable broad-band surface wave dispersion measurements. *Geophysical Journal International*, *169*(3), 1239–1260. doi: 10.1111/j.1365-246X.2007.03374.x

Ben-Zion, Y., & Leary, P. (1986). Thermoelastic strain in a half-space covered by unconsolidated material. *Bulletin of the Seismological Society of America*, *76*(5), 1447–1460. Retrieved from `http://www.bssaonline.org/content/76/5/1447.short`

Berbellini, A., Zaccarelli, L., Faenza, L., Garcia, A., Improta, L., De Gori, P., & Morelli, A. (2021). Effect of Groundwater on Noise-Based Monitoring of Crustal Velocity Changes Near a Produced Water Injection Well in Val d'Agri (Italy). *Frontiers in Earth Science*, *9*(April), 1–13. doi: 10.3389/feart.2021.626720

Berger, J. (1975, 1). A note on thermoelastic strains and tilts. *Journal of Geophysical Research*, *80*(2), 274–277. Retrieved from `http://doi.wiley.com/10.1029/JB080i002p00274` doi: 10.1029/JB080i002p00274

Blewitt, G., Hammond, W. C., & Kreemer, C. (2018). Harnessing the gps data explosion for interdisciplinary science. *Eos*, *99*(10.1029), 485.

Bonilla, L. F., & Ben-Zion, Y. (2021). Detailed space–time variations of the seismic response of the shallow crust to small earthquakes from analysis of dense array data. *Geophysical Journal International*, *225*(1), 298–310.

Bonilla, L. F., Guéguen, P., & Ben-Zion, Y. (2019, 01). Monitoring Coseismic Temporal Changes of Shallow Material during Strong Ground Motion with Interferometry and Autocorrelation. *Bulletin of the Seismological Society of America*, *109*(1), 187-198. Retrieved from `https://doi.org/10.1785/0120180092` doi: 10.1785/0120180092

Borsa, A. A., Agnew, D. C., & Cayan, D. R. (2014). Ongoing drought-induced uplift in the western United States. *Science*, *345*(6204), 1587–1590. Retrieved from `http://www.sciencemag.org/content/345/6204/1587.abstract` doi: 10.1126/science.1260279

Boschelli, J., Moschetti, M. P., & Sens-Schönfelder, C. (2021). Temporal Seismic Velocity Variations: Recovery Following From the 2019 M w 7.1 Ridgecrest, California Earthquake . *Journal of Geophysical Research: Solid Earth*, *126*(4), 1–12. doi: 10.1029/2020jb021465

Brenguier, F., Campillo, M., Hadziioannou, C., Shapiro, N. M., Nadeau, R. M., & Larose, E. (2008, 9). Postseismic Relaxation Along the San Andreas Fault at Parkfield from Continuous Seismological Observations. *Science*, *321*(5895), 1478–1481. Retrieved from `http://www.sciencemag.org/cgi/doi/10.1126/science.1160943` doi: 10.1126/science.1160943

Brenguier, F., Campillo, M., Takeda, T., Aoki, Y., Shapiro, N. M., Briand, X., ... Miyake, H. (2014). Mapping pressurized volcanic fluids from induced crustal seismic velocity drops. *Science*, *345*(6192), 80–82. Retrieved from `http://www.sciencemag.org/content/345/6192/80.abstract` doi: 10.1126/science.1254073

Brenguier, F., Clarke, D., Aoki, Y., Shapiro, N. M., Campillo, M., & Ferrazzini, V. (2011). Monitoring volcanoes using seismic noise correlations. *Comptes Rendus Geoscience*, *343*(8-9), 633–638.

Brenguier, F., Shapiro, N., Campillo, M., Ferrazzini, V., Duputel, Z., Coutant, O., & Nercessian, A. (2008). Towards forecasting volcanic eruptions using seismic noise. *Nature Geoscience*, *1*(2), 126–130. Retrieved from papers://a2ff6e5a-f401-4dac-bc3a-c83939ad6272/Paper/p78 doi: 10.1038/ngeo104

Brodsky, E. E. (2003). A mechanism for sustained groundwater pressure changes induced by distant earthquakes. *Journal of Geophysical Research*, *108*(B8), 1–10. doi: 10.1029/2002JB002321

Budiansky, B., & O'connell, R. J. (1976). Elastic moduli of a cracked solid. *International Journal of Solids and Structures*, *12*(2), 81-97. Retrieved from https://www.sciencedirect.com/science/article/pii/0020768376900445 doi: https://doi.org/10.1016/0020-7683(76)90044-5

Burbey, T. J. (2001, 1). Stress-Strain Analyses for Aquifer-System Characterization. *Groundwater*, *39*(1), 128–136. Retrieved from https://onlinelibrary.wiley.com/doi/abs/10.1111/j.1745-6584.2001.tb00358.x doi: 10.1111/j.1745-6584.2001.tb00358.x

Buwalda, J. (1954). *Geology of the Tehachapi Mountains, California* (Vol. 1; Tech. Rep. No. 170).

California Department of Water Resources. (2015). *California's Most Significant Drought: Comparing Historical and Recent Conditions* (Tech. Rep.). Sacramento, Calififornia: Author.

Carlson, G., Shirzaei, M., Ojha, C., & Werth, S. (2020). Subsidence-derived volumetric strain models for mapping extensional fissures and constraining rock mechanical properties in the san joaquin valley, california. *Journal of Geophysical Research: Solid Earth*, *125*(9), e2020JB019980. Retrieved from https://agupubs.onlinelibrary.wiley.com/doi/abs/10.1029/2020JB019980 (e2020JB019980 2020JB019980) doi: https://doi.org/10.1029/2020JB019980

Castac Basin GSA. (2020). *Groundwater Sustainability Plan Castac Lake Valley* (Tech. Rep.). Castac Basin Ground Water Sustainability.

Claerbout, J., Cole, S., Nichols, D., & Zhang, L. (1988). Why a big 2-D array to record microseisms? *SEP-59*.

Clayton, R. W. (2020, 9). A detailed image of the continent-borderland transition beneath Long Beach, California. *Geophysical Journal International*, *222*(3), 2102–2107. Retrieved from https://academic.oup.com/gji/article/222/3/2102/5856560 doi: 10.1093/gji/ggaa286

Clements, T., & Denolle, M. A. (2018). Tracking Groundwater Levels Using the Ambient Seismic Field. *Geophysical Research Letters*, *45*(13), 6459–6465. doi: 10.1029/2018GL077706

Clements, T., & Denolle, M. A. (2020, 9). SeisNoise.jl: Ambient Seismic Noise Cross Correlation on the CPU and GPU in Julia. *Seismological Research Letters*. Retrieved from https://pubs.geoscienceworld.org/ssa/srl/article/591402/SeisNoisejl-Ambient-Seismic-Noise-Cross doi: 10.1785/0220200192

Compaire, N., Margerin, L., Garcia, R. F., Pinot, B., Calvet, M., Orhand-Mainsant, G., … others (2021). Autocorrelation of the ground vibrations recorded by the seis-insight seismometer on mars. *Journal of Geophysical Research: Planets*, *126*(4), e2020JE006498.

Daly, C., Doggett, M. K., Smith, J. I., Olson, K. V., Halbleib, M. D., Dimcovic, Z., … Kaspar, E. M. (2021). Challenges in observation-based mapping of daily precipitation across the conterminous united states. *Journal of Atmospheric and Oceanic Technology*, *38*(11), 1979 - 1992. Retrieved from https://journals.ametsoc.org/view/journals/atot/38/11/JTECH-D-21-0054.1.xml doi: 10.1175/JTECH-D-21-0054.1

Daly, C., Halbleib, M., Smith, J. I., Gibson, W. P., Doggett, M. K., Taylor, G. H., … Pasteris, P. P. (2008). Physiographically sensitive mapping of climatological temperature and precipitation across the conterminous united states. *International Journal of Climatology*, *28*(15), 2031-2064. Retrieved from `https://rmets.onlinelibrary.wiley.com/doi/abs/10.1002/joc.1688` doi: https://doi.org/10.1002/joc.1688

De Fazio, T. L., Aki, K., & Alba, J. (1973). Solid Earth tide and observed change in the in situ seismic velocity. *Journal of Geophysical Research*, *78*(8), 1319–1322. doi: 10.1029/JB078i008p01319

Delph, J. R., Levander, A., & Niu, F. (2019, 8). Constraining Crustal Properties Using Receiver Functions and the Autocorrelation of Earthquake-Generated Body Waves. *Journal of Geophysical Research: Solid Earth*, *124*(8), 8981–8997. Retrieved from `https://onlinelibrary.wiley.com/doi/10.1029/2019JB017929` doi: 10.1029/2019JB017929

De Plaen, R. S., Lecocq, T., Caudron, C., Ferrazzini, V., & Francis, O. (2016). Single-station monitoring of volcanoes using seismic ambient noise. *Geophysical Research Letters*, *43*(16), 8511–8518. doi: 10.1002/2016GL070078

Dettinger, M. (2016, 7). Historical and Future Relations Between Large Storms and Droughts in California. *San Francisco Estuary and Watershed Science*, *14*(2). Retrieved from `http://escholarship.org/uc/item/1hq3504j` doi: 10.15447/sfews.2016v14iss2art1

Dettinger, M. D., Ralph, F. M., Das, T., Neiman, P. J., & Cayan, D. R. (2011). Atmospheric Rivers, Floods and the Water Resources of California. *Water*, *3*(4), 445–478. Retrieved from `http://www.mdpi.com/2073-4441/3/2/445/` doi: 10.3390/w3020445

Díaz, J., Ruiz, M., Sánchez-Pastor, P. S., & Romero, P. (2017). Urban Seismology: On the origin of earth vibrations within a city. *Scientific Reports*, *7*(1), 1–11. doi: 10.1038/s41598-017-15499-y

Diaz, J., Schimmel, M., Ruiz, M., & Carbonell, R. (2020). Seismometers Within Cities: A Tool to Connect Earth Sciences and Society. *Frontiers in Earth Science*, *8*(February), 1–7. doi: 10.3389/feart.2020.00009

Dodge, D. A., & Beroza, G. C. (1997). Source array analysis of coda waves near the 1989 Loma Prieta, California, mainshock: Implications for the mechanism of coseismic velocity changes. *Journal of Geophysical Research-Solid Earth*, *102*(B11), 24437–24458. doi: 10.1029/97JB02024

Donaldson, C., Winder, T., Caudron, C., & White, R. S. (2019). Crustal seismic velocity responds to a magmatic intrusion and seasonal loading in Iceland's Northern Volcanic Zone. *Science Advances*, *5*(11). doi: 10.1126/sciadv.aax6642

Dong, C., MacDonald, G., Okin, G. S., & Gillespie, T. W. (2019, 12). Quantifying Drought Sensitivity of Mediterranean Climate Vegetation to Recent Warming: A Case Study in Southern California. *Remote Sensing*, *11*(24), 2902. Retrieved from `https://www.mdpi.com/2072-4292/11/24/2902` doi: 10.3390/rs11242902

Famiglietti, J. S., & Rodell, M. (2013, 6). Water in the Balance. *Science*, *340*(6138), 1300–1301. Retrieved from `http://www.sciencemag.org/cgi/doi/10.1126/science.1236460` doi: 10.1126/science.1236460

Feng, K.-F., Huang, H.-H., Hsu, Y.-J., & Wu, Y.-M. (2021). Controls on seasonal variations of crustal seismic velocity in taiwan using single-station cross-component analysis of ambient noise interferometry. *Journal of Geophysical Research: Solid Earth*, *126*(11), e2021JB022650.

Froment, B., Campillo, M., Chen, J. H., & Liu, Q. Y. (2013). Deformation at depth associated with the 12 May 2008 MW 7.9 Wenchuan earthquake from seismic ambient noise monitoring. *Geophysical Research Letters*, *40*(1), 78–82. doi: 10.1029/2012GL053995

Garambois, S., Voisin, C., Romero Guzman, M. A., Brito, D., Guillier, B., & Réfloch, A. (2019). Analysis of ballistic waves in seismic noise monitoring of water table variations in a water field site: Added value from numerical modelling to data understanding. *Geophysical Journal International*, *219*(3), 1636–1647. doi: 10.1093/gji/ggz391

Gassenmeier, M., Sens-Schonfelder, C., Delatre, M., & Korn, M. (2015). Monitoring of Environmental Influences on Seismic Velocity at the Geological Storage Site for CO 2 in Ketzin (Germany) with Ambient Seismic Noise. *Geophysical Journal International*, *200*, 524–533. doi: 10.1093/gji/ggu413

Gassenmeier, M., Sens-Schönfelder, C., Eulenfeld, T., Bartsch, M., Victor, P., Tilmann, F., & Korn, M. (2016). Field observations of seismic velocity changes caused by shaking-induced damage and healing due to mesoscopic nonlinearity. *Geophysical Journal International*, *204*(3), 1490–1502. doi: 10.1093/gji/ggv529

Gonzalez-Ortega, A., Fialko, Y., Sandwell, D., Alejandro Nava-Pichardo, F., Fletcher, J., Gonzalez-Garcia, J., ... Funning, G. (2014). El mayor-cucapah (mw 7.2) earthquake: Early near-field postseismic deformation from insar and gps observations. *Journal of Geophysical Research: Solid Earth*, *119*(2), 1482-1497. Retrieved from `https://agupubs.onlinelibrary.wiley.com/doi/abs/10.1002/2013JB010193` doi: https://doi.org/10.1002/2013JB010193

Gradon, C., Brenguier, F., Stammeijer, J., Mordret, A., Hindriks, K., Campman, X., ... Chmiel, M. (2021). Seismic Velocity Response to Atmospheric Pressure Using Time-Lapse Passive Seismic Interferometry. *Bulletin of the Seismological Society of America*, 1–8. doi: 10.1785/0120210069

Grêt, A., Snieder, R., & Scales, J. (2006). Time-lapse monitoring of rock properties with coda wave interferometry. *Journal of Geophysical Research: Solid Earth*, *111*(3), 1–11. doi: 10.1029/2004JB003354

Gualandi, A., Avouac, J.-P., Michel, S., & Faranda, D. (2020, 7). The predictable chaos of slow earthquakes. *Science Advances*, *6*(27), eaaz5548. Retrieved from `https://advances.sciencemag.org/lookup/doi/10.1126/sciadv.aaz5548` doi: 10.1126/sciadv.aaz5548

Gualandi, A., Liu, Z., & Rollins, C. (2020). Post-large earthquake seismic activities mediated by aseismic deformation processes. *Earth and Planetary Science Letters*, *530*, 115870. Retrieved from `https://www.sciencedirect.com/science/article/pii/S0012821X1930562X` doi: https://doi.org/10.1016/j.epsl.2019.115870

Gualandi, A., Serpelloni, E., & Belardinelli, M. E. (2016, 4). Blind source separation problem in GPS time series. *Journal of Geodesy*, *90*(4), 323–341. Retrieved from `http://link.springer.com/10.1007/s00190-015-0875-4` doi: 10.1007/s00190-015-0875-4

Guéguen, P. (2016). Predicting nonlinear site response using spectral acceleration vs pgv/vs30: a case history using the volvi-test site. *Pure and Applied Geophysics*, *173*(6), 2047–2063.

Gutenberg, B., & Richter, C. (1944). Frequency of Earthquakes in California. *Bulletin of the Seismological Society of America*, 185–188.

Hammond, W. C., Blewitt, G., & Kreemer, C. (2016). Gps imaging of vertical land motion in california and nevada: Implications for sierra nevada uplift. *Journal of Geophysical Research: Solid Earth*, *121*(10), 7681-7703. Retrieved from `https://agupubs.onlinelibrary.wiley.com/doi/abs/10.1002/2016JB013458` doi: https://doi.org/10.1002/2016JB013458

Hart, D. J., & Wang, H. F. (2010). Variation of unjacketed pore compressibility using gassmann's equation and an overdetermined set of volumetric poroelastic measurements. *Geophysics*, *75*(1), N9–N18.

Hillers, G., & Ben-Zion, Y. (2011). Seasonal variations of observed noise amplitudes at 2-18 Hz in southern California. *Geophysical Journal International*, *184*(2), 860–868. doi: 10.1111/j.1365-246X.2010.04886.x

Hillers, G., Ben-Zion, Y., Campillo, M., & Zigone, D. (2015). Seasonal variations of seismic velocities in the San Jacinto fault area observed with ambient seismic noise. *Geophysical Journal International*, *202*(2), 920–932. Retrieved from http://gji.oxfordjournals.org/cgi/doi/10.1093/gji/ggv151 doi: 10.1093/gji/ggv151

Hillers, G., Graham, N., Campillo, M., Kedar, S., Landés, M., & Shapiro, N. (2012). Global oceanic microseism sources as seen by seismic arrays and predicted by wave action models. *Geochemistry, Geophysics, Geosystems*, *13*(1). doi: 10.1029/2011GC003875

Hillers, G., Retailleau, L., Campillo, M., Inbal, A., Ampuero, J. P., & Nishimura, T. (2015). In situ observations of velocity changes in response to tidal deformation from analysis of the high-frequency ambient wavefield. *Journal of Geophysical Research: Solid Earth*, *120*(1), 210–225. doi: 10.1002/2014JB011318

Hobiger, M., Wegler, U., Shiomi, K., & Nakahara, H. (2012). Coseismic and postseismic elastic wave velocity variations caused by the 2008 Iwate-Miyagi Nairiku earthquake, Japan. *Journal of Geophysical Research: Solid Earth*, *117*(9), 1–19. doi: 10.1029/2012JB009402

Hobiger, M., Wegler, U., Shiomi, K., & Nakahara, H. (2014). Single-station cross-correlation analysis of ambient seismic noise: Application to stations in the surroundings of the 2008 Iwate-Miyagi Nairiku earthquake. *Geophysical Journal International*, *198*(1), 90–109. doi: 10.1093/gji/ggu115

Hobiger, M., Wegler, U., Shiomi, K., & Nakahara, H. (2016, 5). Coseismic and postseismic velocity changes detected by Passive Image Interferometry: comparison of one great and five strong earthquakes in Japan. *Geophysical Journal International*, *205*(2), 1053–1073. Retrieved from https://academic.oup.com/gji/article-lookup/doi/10.1093/gji/ggw066 doi: 10.1093/gji/ggw066

Hu, X., Bürgmann, R., Xu, X., Fielding, E., & Liu, Z. (2021). Machine-learning characterization of tectonic, hydrological and anthropogenic sources of active ground deformation in california. *Journal of Geophysical Research: Solid Earth*, *126*(11), e2021JB022373. Retrieved from https://agupubs.onlinelibrary.wiley.com/doi/abs/10.1029/2021JB022373 (e2021JB022373 2021JB022373) doi: https://doi.org/10.1029/2021JB022373

Hughes, D. S., & Kelly, J. L. (1953, 12). Second-Order Elastic Deformation of Solids. *Physical Review*, *92*(5), 1145–1149. Retrieved from https://link.aps.org/doi/10.1103/PhysRev.92.1145 doi: 10.1103/PhysRev.92.1145

Hutton, K., Woessner, J., & Hauksson, E. (2010, 4). Earthquake Monitoring in Southern California for Seventy-Seven Years (1932-2008). *Bulletin of the Seismological Society of America*, *100*(2), 423–446. Retrieved from https://pubs.geoscienceworld.org/bssa/article/100/2/423-446/349275 doi: 10.1785/0120090130

Ikeda, H., & Takagi, R. (2019). Coseismic changes in subsurface structure associated with the 2018 hokkaido eastern iburi earthquake detected using autocorrelation analysis of ambient seismic noise. *Earth, Planets and Space*, *71*(1), 1–11.

Illien, L., Andermann, C., Sens-Schönfelder, C., Cook, K. L., Baidya, K. P., Adhikari, L. B., & Hovius, N. (2021). Subsurface Moisture Regulates Himalayan Groundwater Storage and Discharge. *AGU Advances*, *2*(2). doi: 10.1029/2021av000398

Illien, L., Sens-Schönfelder, C., Andermann, C., Marc, O., Cook, K. L., Adhikari, L. B., & Hovius, N. (2022). Seismic velocity recovery in the subsurface: Transient damage and groundwater drainage following the 2015 gorkha earthquake, nepal. *Journal of Geophysical Research: Solid Earth*, *127*(2), e2021JB023402. Retrieved from https://agupubs.onlinelibrary.wiley.com/doi/abs/10.1029/2021JB023402 (e2021JB023402 2021JB023402) doi: https://doi.org/10.1029/2021JB023402

James, S. R., Knox, H. A., Abbott, R. E., & Screaton, E. J. (2017). Improved moving window cross-spectral analysis for resolving large temporal seismic velocity changes in permafrost. *Geophysical Research Letters*, *44*(9), 4018–4026. doi: 10.1002/2016GL072468

Johnson, K. M., Hammond, W. C., Burgette, R. J., Marshall, S. T., & Sorlien, C. C. (2020). Present-day and long-term uplift across the western transverse ranges of southern california. *Journal of Geophysical Research: Solid Earth*, *125*(8), e2020JB019672. Retrieved from `https://agupubs.onlinelibrary.wiley.com/doi/abs/10.1029/2020JB019672` (e2020JB019672 2020JB019672) doi: https://doi.org/10.1029/2020JB019672

Johnson, P. A., & Jia, X. (2005). Nonlinear dynamics, granular media and dynamic earthquake triggering. *Nature*, *437*(7060), 871–874.

Johnson, P. a., & McEvilly, T. V. (1995, 7). Parkfield seismicity: Fluid-driven? *Journal of Geophysical Research: Solid Earth*, *100*(B7), 12937–12950. Retrieved from `http://doi.wiley.com/10.1029/95JB00474` doi: 10.1029/95JB00474

Johnson, P. A., & Rasolofosaon, P. N. J. (1996, 2). Nonlinear elasticity and stress-induced anisotropy in rock. *Journal of Geophysical Research: Solid Earth*, *101*(B2), 3113–3124. Retrieved from `http://doi.wiley.com/10.1029/95JB02880` doi: 10.1029/95JB02880

Jones, J. P., Okubo, K., Clements, T., & Denolle, M. A. (2020, 4). SeisIO: A Fast, Efficient Geophysical Data Architecture for the Julia Language. *Seismological Research Letters*. Retrieved from `https://pubs.geoscienceworld.org/ssa/srl/article/583741/SeisIO-A-Fast-Efficient-Geophysical-Data` doi: 10.1785/0220190295

Kaproth, B. M., & Marone, C. (2013). Slow earthquakes, preseismic velocity changes, and the origin of slow frictional stick-slip. *Science*, *341*(6151), 1229–1232.

Kim, D., & Lekic, V. (2019). Groundwater variations from autocorrelation and receiver functions. *Geophysical Research Letters*, *46*(23), 13722–13729. doi: 10.1029/2019GL084719

King, N. E., Argus, D., Langbein, J., Agnew, D. C., Bawden, G., Dollar, R. S., ... Barseghian, D. (2007). Space geodetic observation of expansion of the San Gabriel Valley, California, aquifer system, during heavy rainfall in winter 2004-2005. *Journal of Geophysical Research: Solid Earth*, *112*(3), 1–11. doi: 10.1029/2006JB004448

Klein, E., Bock, Y., Xu, X., Sandwell, D. T., Golriz, D., Fang, P., & Su, L. (2019, 11). Transient Deformation in California From Two Decades of GPS Displacements: Implications for a Three-Dimensional Kinematic Reference Frame. *Journal of Geophysical Research: Solid Earth*, *124*(11), 12189–12223. Retrieved from `https://onlinelibrary.wiley.com/doi/10.1029/2018JB017201` doi: 10.1029/2018JB017201

Kuang, X., Jiao, J. J., Zheng, C., Cherry, J. A., & Li, H. (2020). A review of specific storage in aquifers. *Journal of Hydrology*, *581*, 124383. Retrieved from `https://www.sciencedirect.com/science/article/pii/S0022169419311187` doi: https://doi.org/10.1016/j.jhydrol.2019.124383

Larose, E., & Hall, S. (2009, 4). Monitoring stress related velocity variation in concrete with a 2×105 relative resolution using diffuse ultrasound. *The Journal of the Acoustical Society of America*, *125*(4), 1853–1856. Retrieved from `http://asa.scitation.org/doi/10.1121/1.3079771` doi: 10.1121/1.3079771

Lecocq, T., Caudron, C., & Brenguier, F. (2014). MSNoise, a Python Package for Monitoring Seismic Velocity Changes Using Ambient Seismic Noise. *Seismological Research Letters*, *85*(3), 715–726. Retrieved from `http://srl.geoscienceworld.org/cgi/doi/10.1785/0220130073` doi: 10.1785/0220130073

Lecocq, T., Longuevergne, L., Pedersen, H. A., Brenguier, F., & Stammler, K. (2017). Monitoring ground water storage at mesoscale using seismic noise: 30 years of continuous observation and thermo-elastic and hydrological modeling. *Scientific Reports*, *7*(1), 1–16. Retrieved from `http://dx.doi.org/`

10.1038/s41598-017-14468-9 doi: 10.1038/s41598-017-14468-9

Liu, C., Aslam, K., & Daub, E. (2020). Seismic Velocity Changes Caused by Water Table Fluctuation in the New Madrid Seismic Zone and Mississippi Embayment. *Journal of Geophysical Research: Solid Earth*, *125*(8), 1–13. doi: 10.1029/2020JB019524

Lobkis, O. I., & Weaver, R. L. (2003). Coda-wave interferometry in finite solids: Recovery of p-to-s conversion rates in an elastodynamic billiard. *Physical review letters*, *90*(25), 254302.

Lu, Y., & Ben-Zion, Y. (2022). Regional seismic velocity changes following the 2019 m w 7.1 ridgecrest, california earthquake from autocorrelations and p/s converted waves. *Geophysical Journal International*, *228*(1), 620–630.

Machacca-Puma, R., Lesage, P., Larose, E., Lacroix, P., & Anccasi-Figueroa, R. M. (2019). Detection of pre-eruptive seismic velocity variations at an andesitic volcano using ambient noise correlation on 3-component stations: Ubinas volcano, peru, 2014. *Journal of Volcanology and Geothermal Research*, *381*, 83-100. Retrieved from https://www.sciencedirect.com/science/article/pii/S0377027318305614 doi: https://doi.org/10.1016/j.jvolgeores.2019.05.014

Makhnenko, R., & Labuz, J. F. (2013). Saturation of porous rock and measurement of the b coefficient. In *47th us rock mechanics/geomechanics symposium.*

Makhnenko, R. Y., & Labuz, J. F. (2016). Elastic and inelastic deformation of fluid-saturated rock. *Philosophical Transactions of the Royal Society A: Mathematical, Physical and Engineering Sciences*, *374*(2078), 20150422. Retrieved from https://royalsocietypublishing.org/doi/abs/10.1098/rsta.2015.0422 doi: 10.1098/rsta.2015.0422

Mao, S., Campillo, M., Hilst, R. D., Brenguier, F., Stehly, L., & Hillers, G. (2019, 1). High Temporal Resolution Monitoring of Small Variations in Crustal Strain by Dense Seismic Arrays. *Geophysical Research Letters*, *46*(1), 128–137. Retrieved from https://onlinelibrary.wiley.com/doi/abs/10.1029/2018GL079944 doi: 10.1029/2018GL079944

Mao, S., Lecointre, A., van der Hilst, R. D., & Campillo, M. (2022). Space-time monitoring of groundwater fluctuations with passive seismic interferometry. *Nature Communications*, *13*(1), 1–9.

Mao, S., Mordret, A., Campillo, M., Fang, H., & van der Hilst, R. D. (2020). On the measurement of seismic traveltime changes in the time-frequency domain with wavelet cross-spectrum analysis. *Geophysical Journal International*, *221*(1), 550–568. doi: 10.1093/gji/ggz495

Marc, O., Sens-Schönfelder, C., Illien, L., Meunier, P., Hobiger, M., Sawazaki, K., ... Hovius, N. (2021). Toward Using Seismic Interferometry to Quantify Landscape Mechanical Variations after Earthquakes. *Bulletin of the Seismological Society of America*, 1–19. doi: 10.1785/0120200264

Meier, U., Shapiro, N. M., & Brenguier, F. (2010). Detecting seasonal variations in seismic velocities within Los Angeles basin from correlations of ambient seismic noise. *Geophysical Journal International*, *181*(2), 985–996. doi: 10.1111/j.1365-246X.2010.04550.x

Meltzer, A., Rudnick, R., Zeitler, P., Levander, A., Humphreys, G., Karlstrom, K., ... others (1999). The usarray initiative. *Geological Society of America Today*, *9*, 8–10.

Mikesell, T. D., Malcolm, A. E., Yang, D., & Haney, M. M. (2015). A comparison of methods to estimate seismic phase delays: Numerical examples for coda wave interferometry. *Geophysical Journal International*, *202*(1), 347–360. doi: 10.1093/gji/ggv138

Miller, C. D. (1989). Potential hazards from future volcanic eruptions in California. *US Geological Survey Bulletin*, *1847*.

Minato, S., Tsuji, T., Ohmi, S., & Matsuoka, T. (2012). Monitoring seismic velocity change caused by the 2011 tohoku-oki earthquake using ambient noise records.

Geophysical Research Letters, *39*(9).
Mogensen, P. K., & Riseth, A. N. (2018). Optim: A mathematical optimization package for Julia. *Journal of Open Source Software*, *3*(24), 615. doi: 10.21105/joss.00615
Montgomery-Brown, E. K., Wicks, C. W., Cervelli, P. F., Langbein, J. O., Svarc, J. L., Shelly, D. R., . . . Lisowski, M. (2015). Renewed inflation of long valley caldera, california (2011 to 2014). *Geophysical Research Letters*, *42*(13), 5250-5257. Retrieved from `https://agupubs.onlinelibrary.wiley.com/doi/abs/10.1002/2015GL064338` doi: https://doi.org/10.1002/2015GL064338
Mordret, A., Jolly, A. D., Duputel, Z., & Fournier, N. (2010). Monitoring of phreatic eruptions using Interferometry on Retrieved Cross-Correlation Function from Ambient Seismic Noise: Results from Mt. Ruapehu, New Zealand. *Journal of Volcanology and Geothermal Research*, *191*(1-2), 46–59. Retrieved from `http://dx.doi.org/10.1016/j.jvolgeores.2010.01.010` doi: 10.1016/j.jvolgeores.2010.01.010
Nakata, N., & Snieder, R. (2012, 1). Estimating near-surface shear wave velocities in Japan by applying seismic interferometry to KiK-net data. *Journal of Geophysical Research: Solid Earth*, *117*(B1), n/a-n/a. Retrieved from `http://doi.wiley.com/10.1029/2011JB008595` doi: 10.1029/2011JB008595
National Oceanic and Atmospheric Administration. (2005). *The Second Wettest Rainfall Season in Los Angeles Come to an End* (Tech. Rep.). Oxnard, CA. Retrieved from `https://nwschat.weather.gov/p.php?pid=202005261820-KEWX-NOUS44-PNSEWX`
Nishimura, T., Tanaka, S., Yamawaki, T., Yamamoto, H., Sano, T., Sato, M., . . . Sato, H. (2005). Temporal changes in seismic velocity of the crust around Iwate volcano, Japan, as inferred from analyses of repeated active seismic experiment data from 1998 to 2003. *Earth, Planets and Space*, *57*(6), 491–505. doi: 10.1186/BF03352583
Niu, F., Silver, P. G., Daley, T. M., Cheng, X., & Majer, E. L. (2008). Preseismic velocity changes observed from active source monitoring at the parkfield safod drill site. *Nature*, *454*(7201), 204–208.
Nur, A., & Simmons, G. (1969a). The effect of saturation on velocity in low porosity rocks. *Earth and Planetary Science Letters*, *7*(2), 99–108. doi: 10.1016/0012-821X(69)90035-1
Nur, A., & Simmons, G. (1969b). Stress-induced velocity anisotropy in rock: An experimental study. *Journal of Geophysical Research*, *74*(27), 6667. doi: 10.1029/JB074i027p06667
Obermann, A., Froment, B., Campillo, M., Larose, E., Planès, T., Valette, B., . . . Liu, Q. Y. (2014, 4). Seismic noise correlations to image structural and mechanical changes associated with the M w 7.9 2008 Wenchuan earthquake. *Journal of Geophysical Research: Solid Earth*, *119*(4), 3155–3168. Retrieved from `http://doi.wiley.com/10.1002/2013JB010932` doi: 10.1002/2013JB010932
Obermann, A., & Hillers, G. (2019). Seismic time-lapse interferometry across scales. *Advances in Geosciences*, *60*.
Obermann, A., Planès, T., Hadziioannou, C., & Campillo, M. (2016, 10). Lapse-time-dependent coda-wave depth sensitivity to local velocity perturbations in 3-D heterogeneous elastic media. *Geophysical Journal International*, *207*(1), 59–66. Retrieved from `https://academic.oup.com/gji/article-lookup/doi/10.1093/gji/ggw264` doi: 10.1093/gji/ggw264
Obermann, A., Planès, T., Larose, E., & Campillo, M. (2013). Imaging preeruptive and coeruptive structural and mechanical changes of a volcano with ambient seismic noise. *Journal of Geophysical Research: Solid Earth*, *118*(12), 6285–6294.
Obermann, A., Planès, T., Larose, E., Sens-Schönfelder, C., & Campillo, M. (2013).

Depth sensitivity of seismic coda waves to velocity perturbations in an elastic heterogeneous medium. *Geophysical Journal International*, *194*(1), 372–382. doi: 10.1093/gji/ggt043

O'Connell, R. J., & Budiansky, B. (1974, 12). Seismic velocities in dry and saturated cracked solids. *Journal of Geophysical Research*, *79*(35), 5412–5426. Retrieved from `http://doi.wiley.com/10.1029/JB079i035p05412` doi: 10.1029/JB079i035p05412

Ojha, C., Shirzaei, M., Werth, S., Argus, D. F., & Farr, T. G. (2018, 7). Sustained Groundwater Loss in California's Central Valley Exacerbated by Intense Drought Periods. *Water Resources Research*, *54*(7), 4449–4460. Retrieved from `https://onlinelibrary.wiley.com/doi/abs/10.1029/2017WR022250` doi: 10.1029/2017WR022250

Olivier, G., & Brenguier, F. (2016). Interpreting seismic velocity changes observed with ambient seismic noise correlations. *Http://Www.Seg.Org/Interpretation*, *4*(3), 77–85. doi: 10.1190/INT-2015-0203.1

Ostrovsky, L. A., & Johnson, P. A. (2001, 7). Dynamic nonlinear elasticity in geomaterials. *La Rivista del Nuovo Cimento*, *24*(7), 1–46. Retrieved from `http://link.springer.com/10.1007/BF03548898` doi: 10.1007/BF03548898

Passive seismic monitoring with nonstationary noise sources. (2017). *Geophysics*, *82*(4), KS57–KS70.

Pavlis, G. L., & Vernon, F. L. (2010). Array processing of teleseismic body waves with the usarray. *Computers & Geosciences*, *36*(7), 910–920.

Payan, C., Garnier, V., Moysan, J., & Johnson, P. A. (2009, 1). Determination of third order elastic constants in a complex solid applying coda wave interferometry. *Applied Physics Letters*, *94*(1), 011904. Retrieved from `http://aip.scitation.org/doi/10.1063/1.3064129` doi: 10.1063/1.3064129

Peng, Z., & Ben-Zion, Y. (2006). Temporal changes of shallow seismic velocity around the Karadere-Düzce branch of the north Anatolian fault and strong ground motion. *Pure and Applied Geophysics*, *163*(2-3), 567–600. doi: 10.1007/s00024-005-0034-6

Perrone, D., & Jasechko, S. (2017). Dry groundwater wells in the western United States. *Environmental Research Letters*, *12*(10). doi: 10.1088/1748-9326/aa8ac0

Pimienta, L., Fortin, J., & Guéguen, Y. (2017). New method for measuring compressibility and poroelasticity coefficients in porous and permeable rocks. *Journal of Geophysical Research: Solid Earth*, *122*(4), 2670-2689. Retrieved from `https://agupubs.onlinelibrary.wiley.com/doi/abs/10.1002/2016JB013791` doi: https://doi.org/10.1002/2016JB013791

Poupinet, G., Ellsworth, W. L., & Frechet, J. (1984). Monitoring velocity variations in the crust using earthquake doublets: An application to the Calaveras Fault, California. *Journal of Geophysical Research*, *89*(B7), 5719. doi: 10.1029/JB089iB07p05719

Qiu, H., Hillers, G., & Ben-Zion, Y. (2020). Temporal changes of seismic velocities in the San Jacinto Fault zone associated with the 2016 Mw 5.2 Borrego Springs earthquake. *Geophysical Journal International*, *220*(3), 1536–1554. doi: 10.1093/gji/ggz538

Ralph, F. M., & Dettinger, M. D. (2011). Storms, floods, and the science of atmospheric rivers. *Eos*, *92*(32), 265–266. doi: 10.1029/2011EO320001

Ralph, F. M., Neiman, P. J., Kiladis, G. N., Weickmann, K., & Reynolds, D. W. (2011, 4). A Multiscale Observational Case Study of a Pacific Atmospheric River Exhibiting Tropical–Extratropical Connections and a Mesoscale Frontal Wave. *Monthly Weather Review*, *139*(4), 1169–1189. Retrieved from `https://journals.ametsoc.org/doi/10.1175/2010MWR3596.1` doi: 10.1175/2010MWR3596.1

Reasenberg, P. A., & Aki, K. (1974). A precise, continuous measurement of seismic velocity for monitoring in situ stress. *Journal of Geophysical Research*, *79*(2), 399–406. doi: 10.1029/JB079i002p00399

Riahi, N., & Gerstoft, P. (2015). The seismic traffic footprint: Tracking trains, aircraft, and cars seismically. *Geophysical Research Letters*, *42*(8), 2674–2681. doi: 10.1002/2015GL063558

Rice, J. R., & Cleary, M. P. (1976). Diffusion Solutions for Fluid-Saturated Elastic Porous M Constituents. *Reviews of Geophysics and Space Sciences*, *14*(2), 227–241.

Richter, T., Sens-Schönfelder, C., Kind, R., & Asch, G. (2014). Comprehensive observation and modeling of earthquake and temperature-related seismic velocity changes in northern Chile with passive image interferometry. *Journal of Geophysical Research: Solid Earth*, *119*(6), 4747–4765. doi: 10.1002/2013JB010695

Richter, T., Sens-Schönfelder, C., Kind, R., & Asch, G. (2014). Comprehensive observation and modeling of earthquake and temperature-related seismic velocity changes in northern chile with passive image interferometry. *Journal of Geophysical Research: Solid Earth*, *119*(6), 4747–4765.

Riley, F. S. (1969). Analysis of Borehole Extensometer Data from Central California. *International Association of Hydrologic Sciences*, 423–431.

Rivet, D., Brenguier, F., & Cappa, F. (2015). Improved detection of preeruptive seismic velocity drops at the Piton de la Fournaise volcano. *Geophysical Research Letters*, *42*(15), 6332–6339. doi: 10.1002/2015GL064835

Rivet, D., Campillo, M., Radiguet, M., Zigone, D., Cruz-Atienza, V., Shapiro, N. M., ... others (2014). Seismic velocity changes, strain rate and non-volcanic tremors during the 2009–2010 slow slip event in guerrero, mexico. *Geophysical Journal International*, *196*(1), 447–460.

Rivière, J., Shokouhi, P., Guyer, R. A., & Johnson, P. A. (2015). A set of measures for the systematic classification of the nonlinear elastic behavior of disparate rocks. *Journal of Geophysical Research: Solid Earth*, *120*(3), 1587-1604. Retrieved from `https://agupubs.onlinelibrary.wiley.com/doi/abs/10.1002/2014JB011718` doi: https://doi.org/10.1002/2014JB011718

Robeson, S. M. (2015, 8). Revisiting the recent California drought as an extreme value. *Geophysical Research Letters*, *42*(16), 6771–6779. Retrieved from `https://onlinelibrary.wiley.com/doi/abs/10.1002/2015GL064593` doi: 10.1002/2015GL064593

Rodríguez Tribaldos, V., & Ajo-Franklin, J. B. (2021, 4). Aquifer Monitoring Using Ambient Seismic Noise Recorded With Distributed Acoustic Sensing (DAS) Deployed on Dark Fiber. *Journal of Geophysical Research: Solid Earth*, *126*(4), 1–20. Retrieved from `https://onlinelibrary.wiley.com/doi/10.1029/2020JB021004` doi: 10.1029/2020JB021004

Roeloffs, E. (1996). Poroelastic Techniques in the Study of Earthquake-Related Hydrologic Phenomena. *Advances in Geophysics*, *38*(C), 135–195. doi: 10.1016/S0065-2687(08)60270-8

Roeloffs, E. A. (1988). Fault stability changes induced beneath a reservoir with cyclic variations in water level. *Journal of Geophysical Research*, *93*(B3), 2107. Retrieved from `http://doi.wiley.com/10.1029/JB093iB03p02107` doi: 10.1029/JB093iB03p02107

Rojstaczer, S., Wolf, S., & Michel, R. (1995, 1). Permeability enhancement in the shallow crust as a cause of earthquake-induced hydrological changes. *Nature*, *373*(6511), 237–239. Retrieved from `http://www.nature.com/articles/373237a0` doi: 10.1038/373237a0

Rubinstein, J. L. (2004). Evidence for Widespread Nonlinear Strong Ground Motion in the MW 6.9 Loma Prieta Earthquake. *Bulletin of the Seismological Society of America*, *94*(5), 1595–1608. doi: 10.1785/012004009

Rubinstein, J. L., & Beroza, G. C. (2005). Depth constraints on nonlinear strong ground motion from the 2004 parkfield earthquake. *Geophysical Research Letters*, *32*(14). Retrieved from https://agupubs.onlinelibrary.wiley.com/doi/abs/10.1029/2005GL023189 doi: https://doi.org/10.1029/2005GL023189

Saltiel, S., Selvadurai, P. A., Bonner, B. P., Glaser, S. D., & Ajo-Franklin, J. B. (2017). Experimental development of low-frequency shear modulus and attenuation measurements in mated rock fractures: Shear mechanics due to asperity contact area changes with normal stress. *GEOPHYSICS*, *82*(2), M19-M36. Retrieved from https://doi.org/10.1190/geo2016-0199.1 doi: 10.1190/geo2016-0199.1

Save, H., Bettadpur, S., & Tapley, B. D. (2016, 10). High-resolution CSR GRACE RL05 mascons. *Journal of Geophysical Research: Solid Earth*, *121*(10), 7547–7569. Retrieved from http://doi.wiley.com/10.1002/2016JB013007 doi: 10.1002/2016JB013007

Sawazaki, K., Saito, T., & Shiomi, K. (2018). Shallow temporal changes in s wave velocity and polarization anisotropy associated with the 2016 kumamoto earthquake sequence, japan. *Journal of Geophysical Research: Solid Earth*, *123*(11), 9899–9913.

Saygin, E., Cummins, P. R., & Lumley, D. (2017, 1). Retrieval of the P wave reflectivity response from autocorrelation of seismic noise: Jakarta Basin, Indonesia. *Geophysical Research Letters*, *44*(2), 792–799. Retrieved from http://doi.wiley.com/10.1002/2016GL071363 doi: 10.1002/2016GL071363

Schijns, H., Jackson, I., & Schmitt, D. R. (2018). Shear modulus dispersion in cracked and fluid-saturated quartzites: Experimental observations and modeling. *Journal of Geophysical Research: Solid Earth*, *123*(4), 2825-2840. Retrieved from https://agupubs.onlinelibrary.wiley.com/doi/abs/10.1002/2017JB014633 doi: https://doi.org/10.1002/2017JB014633

Schippkus, S., Garden, M., & Bokelmann, G. (2020, 9). Characteristics of the Ambient Seismic Field on a Large-N Seismic Array in the Vienna Basin. *Seismological Research Letters*, *91*(5), 2803–2816. Retrieved from https://pubs.geoscienceworld.org/ssa/srl/article/91/5/2803/588336/Characteristics-of-the-Ambient-Seismic-Field-on-a doi: 10.1785/0220200153

Schurr, D. P., Kim, J.-Y., Sabra, K. G., & Jacobs, L. J. (2011, 12). Damage detection in concrete using coda wave interferometry. *NDT & E International*, *44*(8), 728–735. Retrieved from http://dx.doi.org/10.1016/j.ndteint.2011.07.009https://linkinghub.elsevier.com/retrieve/pii/S0963869511000983 doi: 10.1016/j.ndteint.2011.07.009

Seats, K. J., Lawrence, J. F., & Prieto, G. A. (2012). Improved ambient noise correlation functions using Welch's method. *Geophysical Journal International*, *188*(2), 513–523. doi: 10.1111/j.1365-246X.2011.05263.x

Segall, P. (2010). *Earthquake and Volcano Deformation* (Vol. 48) (No. 01). Princeton: Princeton University Press. doi: 10.1515/9781400833856

Sens-Schönfelder, C., & Eulenfeld, T. (2019, 4). Probing the in situ Elastic Nonlinearity of Rocks with Earth Tides and Seismic Noise. *Physical Review Letters*, *122*(13), 138501. Retrieved from https://doi.org/10.1103/PhysRevLett.122.138501https://link.aps.org/doi/10.1103/PhysRevLett.122.138501 doi: 10.1103/PhysRevLett.122.138501

Sens-Schönfelder, C., & Wegler, U. (2006). Passive image interferemetry and seasonal variations of seismic velocities at Merapi Volcano, Indonesia. *Geophysical Research Letters*, *33*(21), 1–5. doi: 10.1029/2006GL027797

Shokouhi, P., Rivière, J., Guyer, R. A., & Johnson, P. A. (2017). Slow dynamics of consolidated granular systems: Multi-scale relaxation. *Applied Physics Letters*, *111*(25), 251604. Retrieved from https://doi.org/10.1063/1.5010043 doi: 10.1063/1.5010043

Shokouhi, P., Zoëga, A., & Wiggenhauser, H. (2010). Nondestructive Investigation of Stress-Induced Damage in Concrete. *Advances in Civil Engineering*, *2010*, 1–9. Retrieved from http://www.hindawi.com/journals/ace/2010/740189/ doi: 10.1155/2010/740189

Shreedharan, S., Bolton, D. C., Rivière, J., & Marone, C. (2021). Competition between preslip and deviatoric stress modulates precursors for laboratory earthquakes. *Earth and Planetary Science Letters*, *553*, 116623. Retrieved from https://www.sciencedirect.com/science/article/pii/S0012821X20305677 doi: https://doi.org/10.1016/j.epsl.2020.116623

Shreve, R. L. (1968, 1). The Blackhawk Landslide. In (pp. 1–48). Retrieved from https://pubs.geoscienceworld.org/books/book/226/chapter/3794777/ doi: 10.1130/SPE108-p1

Skempton, A. W. (1954, 12). The Pore-Pressure Coefficients A and B. *Géotechnique*, *4*(4), 143–147. Retrieved from http://www.icevirtuallibrary.com/doi/10.1680/geot.1954.4.4.143 doi: 10.1680/geot.1954.4.4.143

Smail, R. A., Pruitt, A. H., Mitchell, P. D., & Colquhoun, J. B. (2019). Cumulative deviation from moving mean precipitation as a proxy for groundwater level variation in Wisconsin. *Journal of Hydrology X*, *5*(June), 100045. Retrieved from https://doi.org/10.1016/j.hydroa.2019.100045 doi: 10.1016/j.hydroa.2019.100045

Small, P., Gill, D., Maechling, P. J., Taborda, R., Callaghan, S., Jordan, T. H., ... Goulet, C. (2017). The scec unified community velocity model software framework. *Seismological Research Letters*, *88*(6), 1539–1552.

Snieder, R., Grêt, A., Douma, H., & Scales, J. (2002, 3). Coda Wave Interferometry for Estimating Nonlinear Behavior in Seismic Velocity. *Science*, *295*(5563), 2253–2255. Retrieved from http://www.sciencemag.org/cgi/doi/10.1126/science.1070015 doi: 10.1126/science.1070015

Snieder, R., Sens-Schönfelder, C., & Wu, R. (2017, 1). The time dependence of rock healing as a universal relaxation process, a tutorial. *Geophysical Journal International*, *208*(1), 1–9. Retrieved from https://academic.oup.com/gji/article-lookup/doi/10.1093/gji/ggw377 doi: 10.1093/gji/ggw377

Swain, D. L. (2015). A tale of two California droughts: Lessons amidst record warmth and dryness in a region of complex physical and human geography. *Geophysical Research Letters*, *42*(22), 9999–10003. doi: 10.1002/2015GL066628

Swain, D. L., Tsiang, M., Haugen, M., Singh, D., Charland, A., Rajaratnam, B., & Diffenbaugh, N. S. (2014). The Extraordinary California Drought of 2013 / 2014 : Character , Context , and the Role of Climate Change. *Bulletin of the American Meteorological Society*(September), 3–7.

Taira, T., Brenguier, F., & Kong, Q. (2015). Ambient noise-based monitoring of seismic velocity changes associated with the 2014 mw 6.0 south napa earthquake. *Geophysical Research Letters*, *42*(17), 6997–7004. doi: 10.1002/2015GL065308

Takano, T., Nishimura, T., & Nakahara, H. (2017). Seismic velocity changes concentrated at the shallow structure as inferred from correlation analyses of ambient noise during volcano deformation at izu-oshima, japan. *Journal of Geophysical Research: Solid Earth*, *122*(8), 6721–6736.

Takano, T., Nishimura, T., Nakahara, H., Ohta, Y., & Tanaka, S. (2014, 9). Seismic velocity changes caused by the Earth tide: Ambient noise correlation analyses of small-array data. *Geophysical Research Letters*, *41*(17), 6131–6136. Retrieved from http://doi.wiley.com/10.1002/2014GL060690 doi: 10.1002/2014GL060690

Takano, T., Nishimura, T., Nakahara, H., Ueda, H., & Fujita, E. (2019, 3). Sensitivity of Seismic Velocity Changes to the Tidal Strain at Different Lapse Times: Data Analyses of a Small Seismic Array at Izu-Oshima Volcano. *Jour-*

nal of Geophysical Research: Solid Earth, *124*(3), 3011–3023. Retrieved from https://onlinelibrary.wiley.com/doi/abs/10.1029/2018JB016235 doi: 10.1029/2018JB016235

Tallaksen, L. (1995, 2). A review of baseflow recession analysis. *Journal of Hydrology*, *165*(1-4), 349–370. Retrieved from http://linkinghub.elsevier.com/retrieve/pii/002216949592779D doi: 10.1016/0022-1694(95)92779-D

Talwani, P., Chen, L., & Gahalaut, K. (2007). Seismogenic permeability, ks. *Journal of Geophysical Research: Solid Earth*, *112*(7), 1–18. doi: 10.1029/2006JB004665

Tkalčić, H., Phm, T.-S., & Wang, S. (2020). The earth's coda correlation wavefield: Rise of the new paradigm and recent advances. *Earth-Science Reviews*, *208*, 103285.

Toppozada, T. R., Branum, D. M., Reichle, M., & Hallstrom, C. (2002, 10). San Andreas Fault Zone, California: M ¿=5.5 Earthquake History. *Bulletin of the Seismological Society of America*, *92*(7), 2555–2601. Retrieved from https://pubs.geoscienceworld.org/bssa/article/92/7/2555-2601/120726 doi: 10.1785/0120000614

Trifunac, M. D. (2016). Site conditions and earthquake ground motion – a review. *Soil Dynamics and Earthquake Engineering*, *90*, 88-100. Retrieved from https://www.sciencedirect.com/science/article/pii/S026772611630118X doi: https://doi.org/10.1016/j.soildyn.2016.08.003

Tsai, V. C. (2011). A model for seasonal changes in GPS positions and seismic wave speeds due to thermoelastic and hydrologic variations. *Journal of Geophysical Research: Solid Earth*, *116*(4), 1–9. doi: 10.1029/2010JB008156

Ueno, T., Saito, T., Shiomi, K., Enescu, B., Hirose, H., & Obara, K. (2012). Fractional seismic velocity change related to magma intrusions during earthquake swarms in the eastern izu peninsula, central japan. *Journal of Geophysical Research: Solid Earth*, *117*(B12).

Viens, L., Denolle, M. A., Hirata, N., & Nakagawa, S. (2018). Complex Near-Surface Rheology Inferred From the Response of Greater Tokyo to Strong Ground Motions. *Journal of Geophysical Research: Solid Earth*, 5710–5729. doi: 10.1029/2018JB015697

Viens, L., Jiang, C., & Denolle, M. A. (2022). Imaging the kanto basin seismic basement with earthquake and noise autocorrelation functions. *Geophysical Journal International*.

Voisin, C., Garambois, S., Massey, C., & Brossier, R. (2016). Seismic noise monitoring of the water table in a deep-seated, slow-moving landslide. *Interpretation*, *4*(3), SJ67–SJ76.

Voisin, C., Guzmán, M. A. R., Réfloch, A., Taruselli, M., & Garambois, S. (2017). Groundwater Monitoring with Passive Seismic Interferometry. *Journal of Water Resource and Protection*, *09*(12), 1414–1427. Retrieved from http://www.scirp.org/journal/doi.aspx?DOI=10.4236/jwarp.2017.912091 doi: 10.4236/jwarp.2017.912091

von Seggern, D. H., & Anderson, J. G. (2017). Velocity change in the zone of a moderate mw 5.0 earthquake revealed by autocorrelations of ambient noise and by event spectra. *Pure and Applied Geophysics*, *174*(5), 1923–1935.

Wahr, J., Molenaar, M., & Bryan, F. (1998, 12). Time variability of the Earth's gravity field: Hydrological and oceanic effects and their possible detection using GRACE. *Journal of Geophysical Research: Solid Earth*, *103*(B12), 30205–30229. Retrieved from http://doi.wiley.com/10.1029/98JB02844 doi: 10.1029/98JB02844

Wang, Q. Y., Brenguier, F., Campillo, M., Lecointre, A., Takeda, T., & Aoki, Y. (2017). Seasonal Crustal Seismic Velocity Changes Throughout Japan. *Journal of Geophysical Research: Solid Earth*, *122*(10), 7987–8002. doi: 10.1002/2017JB014307

Wang, S.-Y. S., Yoon, J.-H., Becker, E., & Gillies, R. (2017, 7). California from drought to deluge. *Nature Climate Change*, *7*(7), 465–468. Retrieved from http://www.nature.com/articles/nclimate3330 doi: 10.1038/nclimate3330

Webb, S. C. (2007). The earth's 'hum'is driven by ocean waves over the continental shelves. *Nature*, *445*(7129), 754–756. doi: 10.1038/nature05536

Wegler, U., Nakahara, H., Sens-Schönfelder, C., Korn, M., & Shiomi, K. (2009). Sudden drop of seismic velocity after the 2004 Mw 6.6 mid-Niigata earthquake, Japan, observed with Passive Image Interferometry B06305. *Journal of Geophysical Research: Solid Earth*, *114*(6), 1–11. doi: 10.1029/2008JB005869

Wegler, U., & Sens-Schönfelder, C. (2007). Fault zone monitoring with passive image interferometry. *Geophysical Journal International*, *168*(3), 1029–1033. doi: 10.1111/j.1365-246X.2006.03284.x

Wen, Y., Behrangi, A., Chen, H., & Lambrigtsen, B. (2018, 11). How well were the early 2017 California Atmospheric River precipitation events captured by satellite products and ground-based radars? *Quarterly Journal of the Royal Meteorological Society*, *144*(S1), 344–359. Retrieved from https://onlinelibrary.wiley.com/doi/abs/10.1002/qj.3253 doi: 10.1002/qj.3253

Williams, A. P., Abatzoglou, J. T., Gershunov, A., Guzman-Morales, J., Bishop, D. A., Balch, J. K., & Lettenmaier, D. P. (2019, 8). Observed Impacts of Anthropogenic Climate Change on Wildfire in California. *Earth's Future*, *7*(8), 892–910. Retrieved from https://onlinelibrary.wiley.com/doi/abs/10.1029/2019EF001210 doi: 10.1029/2019EF001210

Williams, A. P., Seager, R., Abatzoglou, J. T., Cook, B. I., Smerdon, J. E., & Cook, E. R. (2015). Contribution of anthropogenic warming to california drought during 2012–2014. *Geophysical Research Letters*, *42*(16), 6819–6828.

Wu, C., Delorey, A., Brenguier, F., Hadziioannou, C., Daub, E. G., & Johnson, P. (2016). Constraining depth range of s wave velocity decrease after large earthquakes near parkfield, california. *Geophysical Research Letters*, *43*(12), 6129-6136. Retrieved from https://agupubs.onlinelibrary.wiley.com/doi/abs/10.1002/2016GL069145 doi: https://doi.org/10.1002/2016GL069145

Wu, C., & Peng, Z. (2012). Long-term change of site response after the mw 9.0 tohoku earthquake in japan. *Earth, planets and space*, *64*(12), 1259–1266.

Yamamura, K., Sano, O., Utada, H., Takei, Y., Nakao, S., & Fukao, Y. (2003). Long-term observation of in situ seismic velocity and attenuation. *Journal of Geophysical Research: Solid Earth*, *108*(B6), 1–15. Retrieved from http://doi.wiley.com/10.1029/2002JB002005 doi: 10.1029/2002JB002005

Yang, X., Jared, B., Kurama, O., Jiang, C., Clements, T., & A., D. M. (2022). Optimal Stacking of Noise Cross-Correlation Functions. *in review in Geophysical Journal International*, –.

Yu, E., Bhaskaran, A., Chen, S.-l., Ross, Z. E., Hauksson, E., & Clayton, R. W. (2021, 6). Southern California Earthquake Data Now Available in the AWS Cloud. *Seismological Research Letters*. Retrieved from https://pubs.geoscienceworld.org/srl/article/doi/10.1785/0220210039/600883/Southern-California-Earthquake-Data-Now-Available doi: 10.1785/0220210039

Yuan, C., Bryan, J., & Denolle, M. (2021, 5). Numerical comparison of time-, frequency- and wavelet-domain methods for coda wave interferometry. *Geophysical Journal International*, *226*(2), 828–846. Retrieved from https://academic.oup.com/gji/article/226/2/828/6224864 doi: 10.1093/gji/ggab140

Zhang, Y., Abraham, O., Grondin, F., Loukili, A., Tournat, V., Duff, A. L., … Durand, O. (2012). Study of stress-induced velocity variation in concrete under direct tensile force and monitoring of the damage level by using thermallycompensated Coda Wave Interferometry. *Ultrasonics*, *52*(8), 1038–1045. doi: 10.1016/j.ultras.2012.08.011

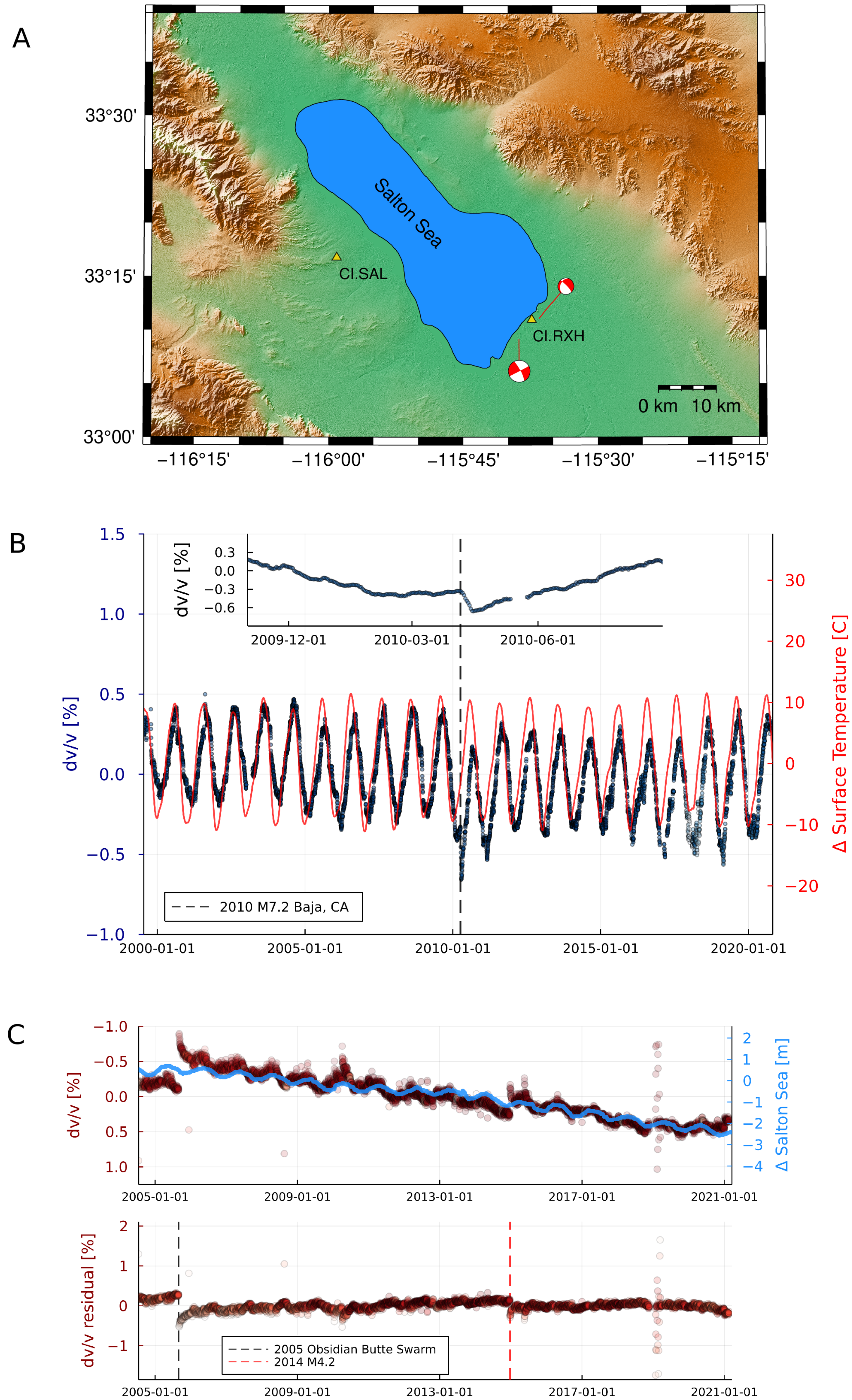

Figure 5. dv/v near the Salton Sea. (a) Location of stations CI.SAL and CI.RXH near the Salton Sea (b) *dv/v* and change in surface temperature at station CI.SAL. The dotted line and inset show the timing of M7.2 El Mayor Cucapah 2010 Earthquake. (c) *dv/v* and change in elevation of the Salton Sea. The dotted lines in lower panel indicate the 2005 Obsidian Butte swarm and a 2014 M4.2 local earthquake, respectively.

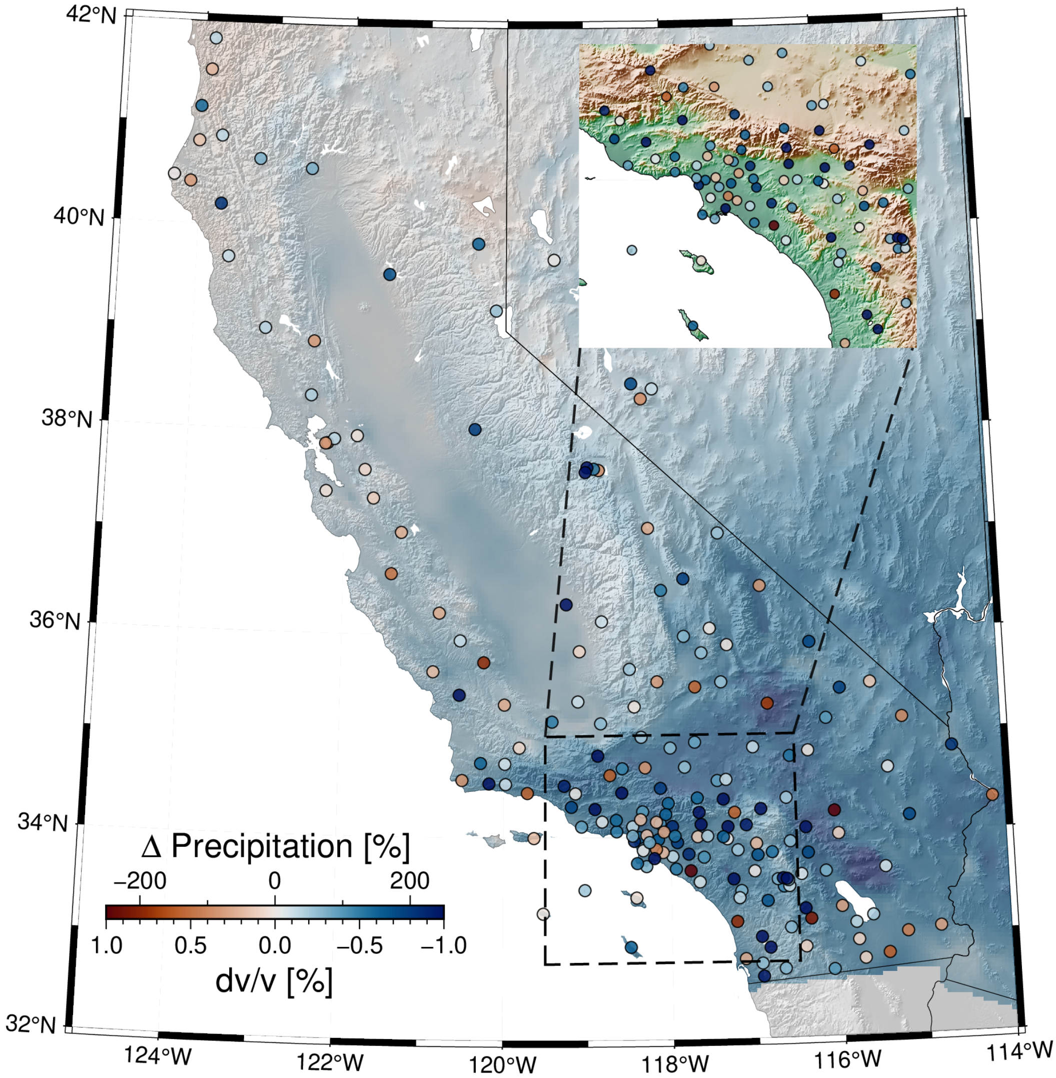

Figure 6. Change in *dv/v* measured as the ratio of *p2p* taken during the 2004-2005 year normalized to the mean of the yearly *p2p* between 1985 and 2020 (scatter points), annual precipitation deficit (colormap) over the same time frame, and topography in relief. The inset map shows a zoom in southern California with topography in colormap and in relief.

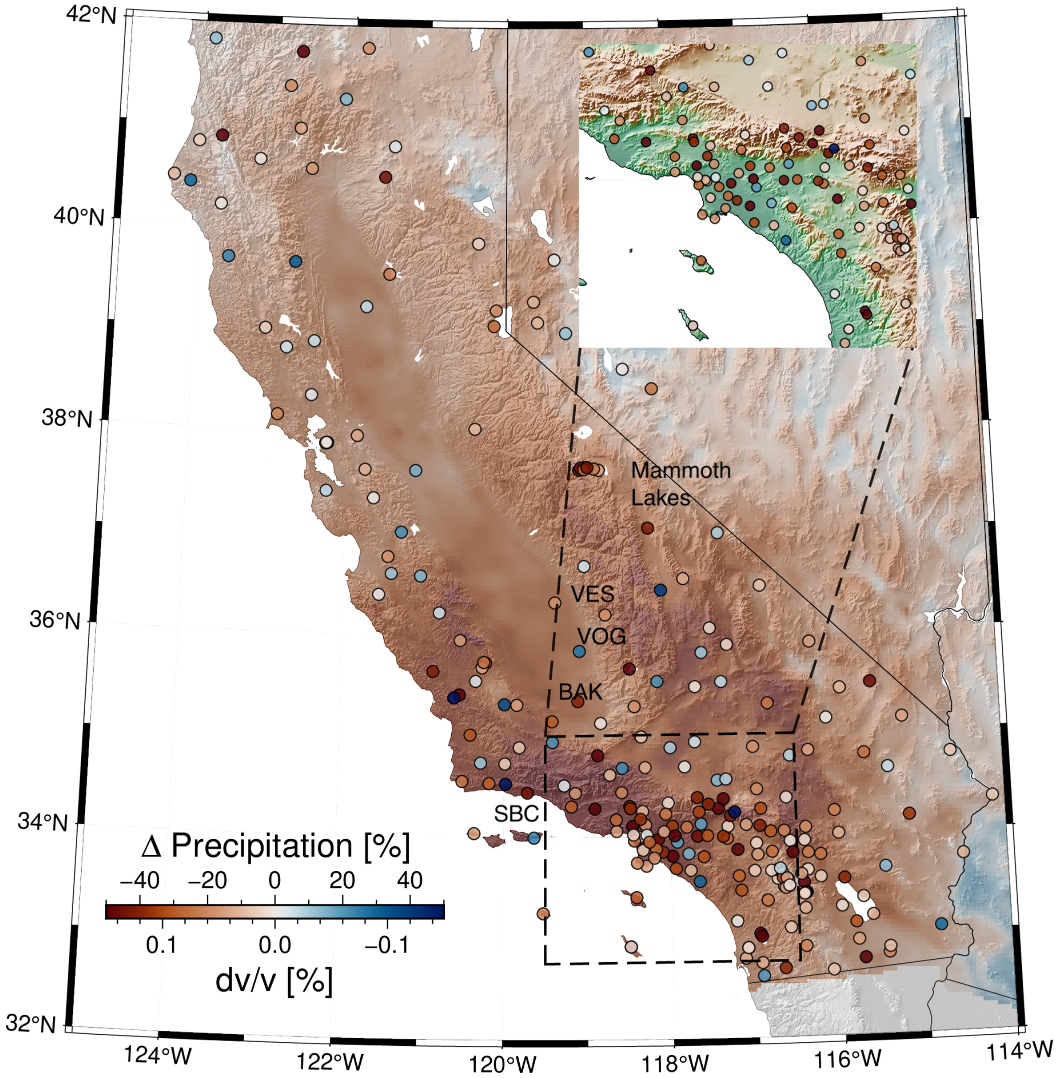

Figure 7. Multi-year annual rate of dv/v as measured by the slope of a linear regression (scatter points) and precipitation deficit (colormap) between October 1^{st}, 2011 and October 1^{st}, 2016. The inset map shows a zoom in southern California with topography in colormap and relief.

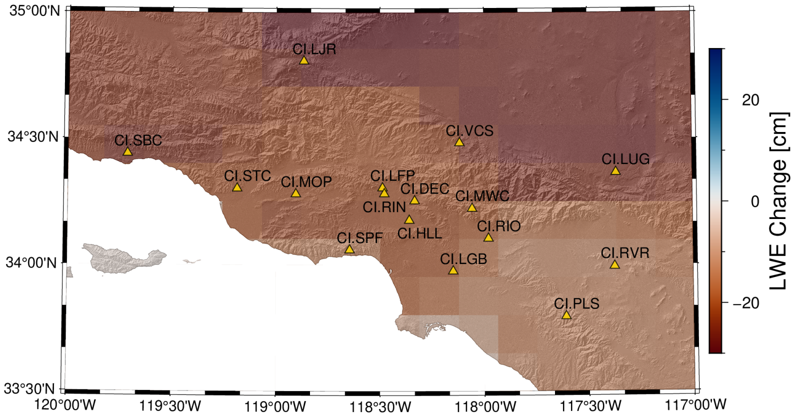

(a)

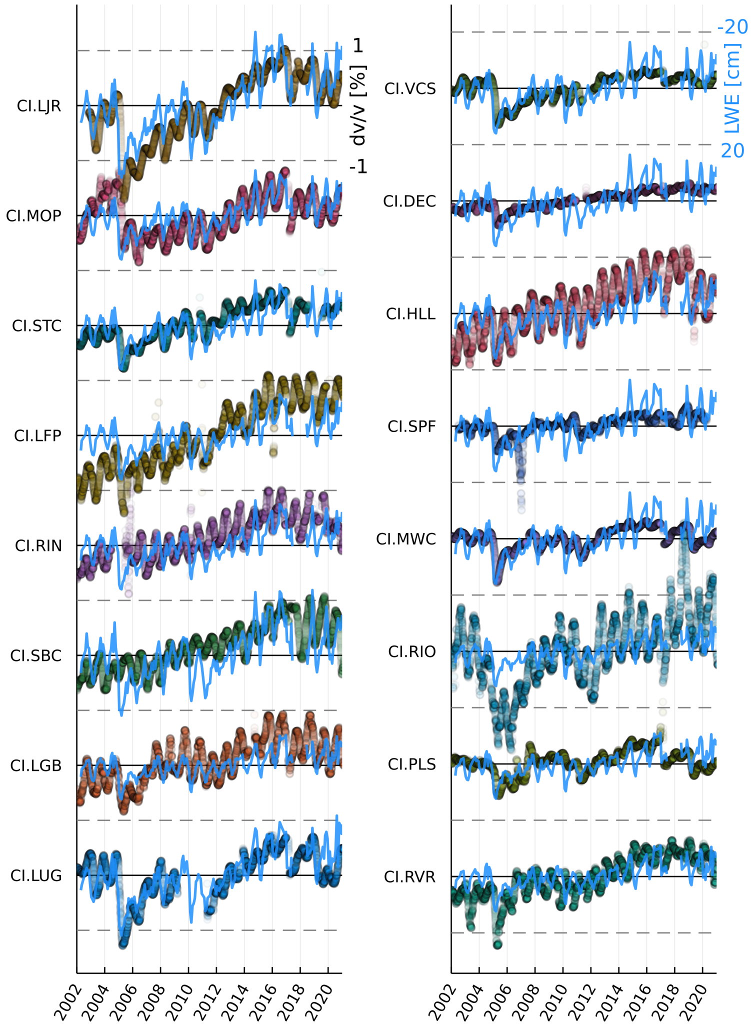

(b)

Figure 8. Changes in GRACE Liquid Water Equivalent and dv/v in Los Angeles area in 2-4 Hz frequency band from 2006 - 2021. (a) Change in Liquid Water Equivalent as measured by GRACE between January 2002 and January 2021 and CI network stations. (b) Change in dv/v at stations shown in (a) and LWE change between these dates and scaled by the factor $1\% dv/v = -20 cm LWE$.

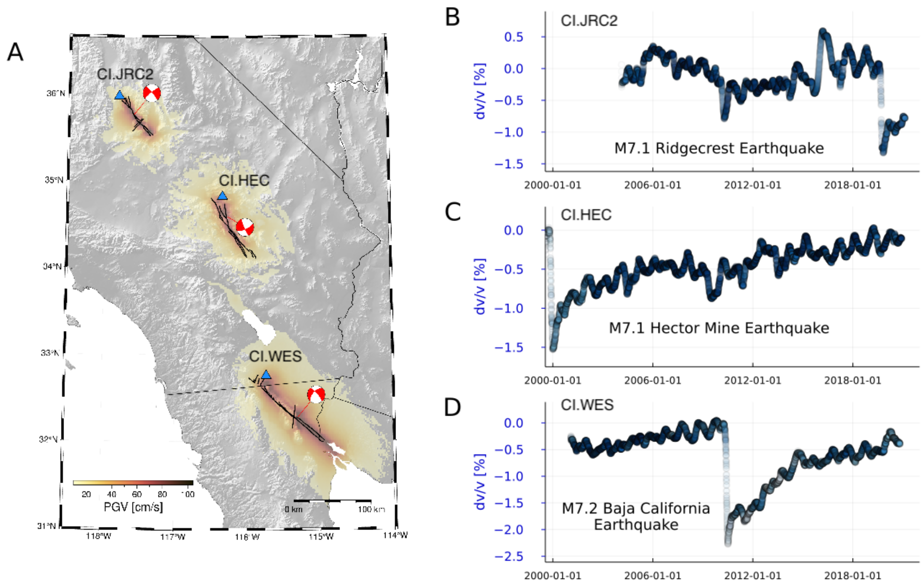

Figure 9. Probing the time scales of post-seismic relaxation processes. (a) Peak ground velocity from the 2019 M7.1 Ridgecrest, 1999 M7.1 Hector Mine and 2010 M7.2 El Mayor-Cucapah earthquakes, respectively, from North to South. Blue triangles indicate the location of nearest seismometers, CI.JRC2, CI.HEC, and CI.WES, that have earthquake signals, respectively from North to South. Focal mechanisms are offset from the epicentral location (from NEIC). (b) *dv/v* times series, after removal of the thermoelastic and hydrological terms of CI.JRC2 (B), CI.HEC (C), and CI.WES (D).